

POLITECNICO DI TORINO

Master's Degree in Mechatronic Engineering



Master's Degree Thesis

**Modelling and design of a reconfigurable
AUV**

Supervisors

Prof.ssa Giuliana Mattiazzo

Prof. Benedetto Allotta

Ing. Fabio Carapellese

Ing. Jonathan Gelli

Candidate

Silvia Bertinetto

April 2025

Abstract

The present study focuses on the modelling and design of a reconfigurable *Autonomous Underwater Vehicle* (AUV), intended for survey and hovering operations. The research activity is divided in two main areas of study: the control of the vehicle in survey configuration and the design of a mechanical assistance system for the reconfiguration process.

The first part involves the development of a dynamic model for the system, with emphasis on kinematics expressed in quaternions, ensuring an efficient and singularity-free representation of rotations. Vehicle control is implemented through a PID controller for trajectory tracking, in order to evaluate the stability and precision of the system along predefined paths. The model validation is carried out via numerical simulations, incorporating the effects of hydrodynamic forces and ocean currents.

The second part addresses a critical issue during configuration changes, focusing on the design of a system based on pulleys' mechanism. Specifically, the study examines the material properties of the rope, the geometry of the pulley to be designed and the structural parameters of the system. Experimental tests on prototypes were conducted to validate the behaviour of the mechanism, with results compared to *Finite Element Method* (FEM) simulations. Finally, two distinct ratchet systems for cable tensioning and final component production are presented.

Acknowledgements

I would like to express my gratitude to Professor Giuliana Mattiazzo and Professor Benedetto Allotta for the remarkable opportunity that allowed me to undertake this thesis. A special thanks to Eng. Fabio Carapellese and Eng. Jonathan Gelli for their guidance and support, which they provided with dedication, enthusiasm, and precision throughout the writing of this thesis.

I am deeply grateful to my family and friends for their unwavering support and encouragement throughout the years of my studies.

Finally, I would like to thank the Team PoliTOcean and the MdM Lab for the incredible opportunities they have given me, allowing me to grow both professionally and personally.

Table of Contents

List of Tables	VIII
List of Figures	IX
Acronyms	XIII
1 Introduction	1
1.1 State of the Art of AUVs	1
1.2 Overall Framework	2
1.2.1 Team PoliTOcean	3
1.2.2 MDM Lab	4
1.3 Thesis Motivation	5
I	8
2 Modelling of the AURV	9
2.1 Notation	10
2.2 Equations of motion	12
2.3 Rigid Body's Kinematics	13
2.3.1 Reference Frames	13
2.3.2 Transformation Between BODY and NED	15
2.4 Rigid Body's Dynamics	16
2.5 Hydrostatics	17
2.6 Hydrodynamics	19
2.6.1 Added Mass and Inertia	19
2.6.2 Damping Effects	21
2.7 Ocean Current Forces and Moments	23
2.7.1 Equation of motion including Ocean Currents	24
2.8 Dynamic parameters of the system	25
2.8.1 Thruster dynamics and Control allocation	25

3	Trajectory Tracking	30
3.1	LOS - Line of Sight	31
3.2	PID controller	33
4	Simulations and results	36
4.1	First trajectory: straight line	36
4.2	Second trajectory: L-shape	37
4.3	Third trajectory: smooth curve	37
4.4	Fourth trajectory: S-path	38
II		45
5	Problem definition	46
6	Pulley design	48
6.1	Rope Material	48
6.2	Pulley groove	49
6.3	Rope parameters	51
6.4	Pulley body	53
7	Beta pulley experimental testing	56
7.1	Dry testing	56
7.2	Validation on FEM simulation studies	59
7.2.1	Simulation with experimental parameters	60
7.2.2	Simulation with theoretical parameters	63
8	Tensioning system	66
8.1	External ratchet system	66
8.2	Internal ratchet system	68
8.2.1	Pulley A	69
8.2.2	Pulley B	69
8.2.3	Design of the ratchet system	70
9	Final considerations	75
9.1	Pulley manufacturing	75
9.2	Final testing	75
10	Conclusions	79

A Rigid-Body dynamics	81
A.1 Newton-Euler formulation	81
A.2 Equation of Motion	85
Bibliography	88

List of Tables

2.1	SNAME notation for marine vessels	11
2.2	RUVIFIST's parameters	26
3.1	PID gains for position and yaw control	35
6.1	<i>Dyneema SK78</i> characteristics	49
7.1	First test	58
7.2	Second test	58
7.3	Third test	58
7.4	Preload values of the rope	59
9.1	Final test	76

List of Figures

1.1	ROV Hercules	2
1.2	AUV Sabertooth	2
1.3	Shape-shifting AUV AQUANAUT	2
1.4	PoliTOcean Student Team	3
1.5	EVA and the float designed for the Mate ROV Competition 2024	4
1.6	AUV FeelHippo	5
1.7	The logo of the ISME consortium	5
1.8	RUVIFIST prototype survey configuration	7
1.9	RUVIFIST prototype hovering configuration	7
2.1	Closed-loop AURV model system simulator scheme	9
2.2	Reference frames	14
2.3	NED and BODY frames of RUVIFIST	14
2.4	Gravitational and buoyancy forces acting on the center of gravity CG and on the center of buoyancy CB of RUVIFIST	18
2.5	Rigid-body and fluid kinetic energy	20
2.6	RUVIFIST schematic of thrust forces w.r.t. CG	27
2.7	T200 BlueRobotics Thrust (kgf) w.r.t. the ESC PWM Input Value (μs)	28
3.1	Block diagram of the LOS guidance for the horizontal plane	30
3.2	LOS geometry for straight lines in the xy plane	33
4.1	First trajectory: evolution of X and Y	39
4.2	First trajectory: trajectories comparison	39
4.3	Second trajectory: evolution of X and Y	40
4.4	Second trajectory: trajectories comparison	40
4.5	First trajectory: propulsion	41
4.6	Second trajectory: propulsion	41
4.7	Third trajectory: evolution of X and Y	42
4.8	Third trajectory: trajectories comparison	42

4.9	Fourth trajectory: evolution of X and Y	43
4.10	Fourth trajectory: trajectories comparison	43
4.11	Third trajectory: propulsion	44
5.1	Survey configuration	47
5.2	Hovering configuration	47
6.1	Cross configuration	49
6.2	Groove parameters scheme	50
6.3	CAD model for the beta test	51
6.4	Beta pulley	53
6.5	Rope configuration scheme	54
6.6	Safety node	54
7.1	Beta pulleys testing	56
7.2	Load cell simulating the external disturbance F_d	56
7.3	Joint configuration	57
7.4	Failure behaviour of the joint during beta testing	60
7.5	Pulley scheme no.1	61
7.6	Pulley scheme no.2	62
7.7	Experimental parameters - displacement along the y direction [mm]	63
7.8	Theoretical parameters - displacement along the y direction [mm]	64
8.1	Exploded view of the pulley	67
8.2	Internal view of the pulley	67
8.3	Ratchet system	67
8.4	In orange, the moving part and the allowed rotation	68
8.5	Ratchet system of <i>Pulley A</i>	69
8.6	Upper view of of <i>Pulley A</i>	69
8.7	Lower view of of <i>Pulley A</i>	69
8.8	Exploded view of the pulley	70
8.9	Internal view of the pulley	70
8.10	Ratchet system	70
8.11	CAD scheme of the ratchet system	71
8.12	Pawl scheme	72
8.13	Stress analysis of the pawl [MPa]	73
8.14	Displacement of the pawl along the radial direction of the tooth [mm]	73
9.1	Metal components of the pulleys	76
9.2	3D printing of the components of the pulleys	76
9.3	Assembled <i>Pulley A</i> (on the right) and <i>Pulley B</i> (on the left)	77
9.4	<i>Pulley A</i> assembled on RUVIFIST for the final test	77

9.5	Final configuration of <i>Pulley A</i> and <i>Pulley B</i>	78
A.1	Kinematics of a particle of the rigid body	83

Acronyms

AURV

Autonomous Reconfigurable Underwater Vehicle

AUV

Autonomous Underwater Vehicle

BF

Body-fixed Frame

CAD

Computer Assisted Design

CB

Center of Buoyancy

CG

Center of Gravity

CO

Geometric Center

DOF

Degree Of Freedom

EUMR

EU Marine Robots

FDM

Fused Deposition Modelling

FEM

Finite Element Method

IF

Inertial Frame

IMU

Inertial Measurement Unit

ISME

Interuniversity Center of Integrated Systems for the Marine Environment

LOS

Line Of Sight

MATE

Marine Advanced Technology Education

MDM

Mechatronics and Dynamic Modelling Laboratory

MPC

Model Predictive Control

NED

North-East-Down

PID

Proportional-Integral-Derivative

PWM

Pulse-Width Modulation

ROV

Remotely Operated Vehicle

SMAME

Society of Naval Architects and Marine Engineers

TCM

Thrust Configuration Matrix

Chapter 1

Introduction

The exploration and study of the underwater world have always presented significant challenges due to the inhospitable nature of these environments. However, advancements in technology have opened up new frontiers, allowing humans to venture into the depths of the ocean without physically entering the water. One remarkable innovation in this field is the development of *Autonomous Underwater Vehicles* (AUVs) [[Figure 1.2], which have significantly expanded the capabilities of underwater operations.

1.1 State of the Art of AUVs

Over the past few decades, the field of underwater robotics has witnessed significant growth, driven by the need for autonomous solutions capable of replacing human operators in complex and hazardous underwater environments. Initially developed for military applications, AUVs have progressively expanded into scientific, industrial, and commercial domains. The offshore oil and gas industry, for example, relies on AUVs for seabed inspections, maintenance, and environmental monitoring, reducing operational costs compared to traditional *Remotely Operated Vehicles* (ROVs) [Figure 1.1].

Most conventional AUVs are designed with a torpedo-like shape to optimize hydrodynamic performance, enabling long-distance navigation with minimal energy consumption. However, these vehicles often lack the maneuverability required for detailed inspections and intervention tasks, which are better suited to stocky, multi-degree-of-freedom ROVs. This trade-off has led to an increasing interest in hybrid solutions, such as *Autonomous Underwater Reconfigurable Vehicles* (AURVs), which can transition between survey-oriented and intervention-focused configurations. Recent advancements in modular marine robotics have introduced promising solutions, such as the *AQUANAUT* by Houston Mechatronics, both capable of

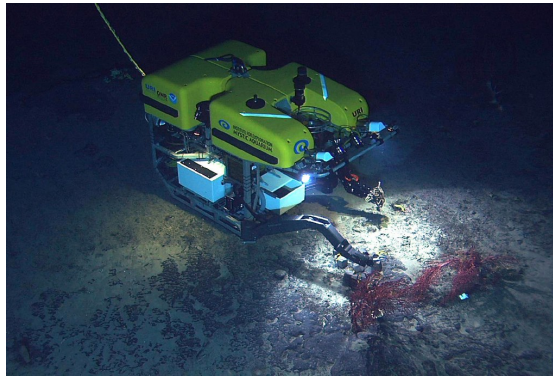


Figure 1.1: ROV Hercules



Figure 1.2: AUV Sabertooth



Figure 1.3: Shape-shifting AUV AQUANAUT

autonomously altering their configurations to perform a variety of underwater tasks [Figure 1.3].

1.2 Overall Framework

The development of AUV technology has been supported by various research groups and institutions worldwide, each contributing to different aspects of marine robotics.

This section introduces two research entities involved in the study of underwater robotic systems: the PoliTOcean team and the MDM Lab. Although these two groups operate independently, their research efforts align with the broader objective of advancing ROVs and AUVs capabilities.

1.2.1 Team PoliTOcean

PoliTOcean is a student-led research group from the Polytechnic University of Turin [Figure 1.4], actively involved in the development of underwater ROVs. The team participates annually in the *Marine Advanced Technology Education* (MATE) ROV Competition, an international event focused on fostering innovation in underwater robotics. Over the years, PoliTOcean has developed several prototypes, including the EVA ROV [Figure 1.5], designed for manipulation tasks at various depths.



Figure 1.4: PoliTOcean Student Team

The EVA prototype is equipped with eight thrusters (T200 by BlueRobotics), allowing for precise maneuverability. Its control system integrates an *Inertial Measurement Unit* (IMU) with a Kalman Filter, a barometer for depth estimation, and two camera modules for real-time visual feedback. The vehicle's mechanical structure is composed of high-density polyethylene (HDPE) and aluminum alloys, ensuring robustness and water resistance up to depths of 300 meters.

PoliTOcean's multidisciplinary approach involves divisions dedicated to mechanics, electronics, firmware, hydrodynamics and control systems, working collaboratively to enhance the performance and stability of their underwater vehicles.

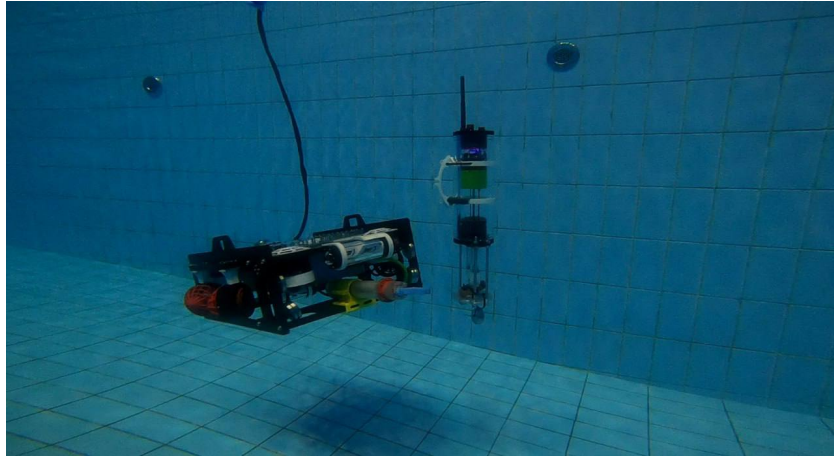


Figure 1.5: EVA and the float designed for the Mate ROV Competition 2024

1.2.2 MDM Lab

The *Mechatronics and Dynamic Modelling Laboratory* (MDM Lab) at the University of Florence (UNIFI DIEF) has been a leading research center in underwater robotics since 2010, specializing in Autonomous Underwater Vehicles (AUVs). Over the years, the laboratory has actively participated in numerous regional, national, and European research projects, significantly advancing the development of autonomous marine systems.

MDM Lab has been involved in several innovative AUV projects, including the development of the *Typhoon* class AUVs and the *Marine Robotic Tool for Archaeology* (MARTA), which was specifically designed for underwater archaeological exploration. The laboratory also contributed to the European FP7 *ARROWS* project, focused on providing low-cost and reliable solutions for marine archaeology. In recent years, MDM Lab has expanded its research to include Autonomous Underwater Reconfigurable Vehicles (AURVs), which are capable of dynamically reconfiguring their structure to optimize performance in different operational scenarios. Among the laboratory's notable contributions is the development of the *FeelHippo* AUV [Figure 1.6], a lightweight, low-cost vehicle designed to be a versatile platform for a variety of research tasks. This vehicle, which is part of the lab's AUV fleet, exemplifies MDM Lab's commitment to creating efficient and flexible robotic systems capable of addressing a broad range of underwater exploration challenges.

In 2014, MDM Lab became a member of the *Interuniversity Center of Integrated Systems for the Marine Environment* (ISME) [Figure 1.7], a consortium of Italian academic institutions dedicated to advancing marine robotics. This collaboration

has allowed MDM Lab to carry out large-scale experimental campaigns in partnership with industrial entities such as the Naval Support and Experimentation Center (CSSN) of the Italian Navy. Moreover, MDM Lab's involvement in the H2020 *EU Marine Robots* (EUMR) initiative has further strengthened European research infrastructures in the field of marine robotics.



Figure 1.6: AUV FeelHippo



Figure 1.7: The logo of the ISME consortium

1.3 Thesis Motivation

In this study, I will apply the knowledge gained during my time at PoliTOcean to work on a new prototype of an AURV patented by the MDM Lab, namely RUVIFIST [1] [2] [3] [4] [5]. The primary objective of this thesis is to explore new methodologies for enhancing the versatility of AUVs through reconfigurable designs. The motivation comes from the increasing demand for adaptable underwater vehicles capable of performing both survey and hovering tasks within a single mission. Traditional AUVs are often optimized for either long-range navigation or precision

maneuvering, leading to operational constraints. By investigating reconfigurable architectures, this research aims to bridge the gap between these two operational modes, offering a solution that maximizes both efficiency and maneuverability in diverse underwater environments. This thesis aims to contribute to the field of underwater robotics by focusing on the design and control of a reconfigurable AUV capable of transitioning between survey and hovering configurations. By leveraging advanced modelling techniques and control strategies, this study seeks to enhance the adaptability and efficiency of AUVs in diverse underwater missions. The collaboration between different research entities, such as PoliTOcean and MDM Lab, highlights the multidisciplinary nature of this field, where innovative solutions emerge from the intersection of mechanical design, control theory, and marine engineering.

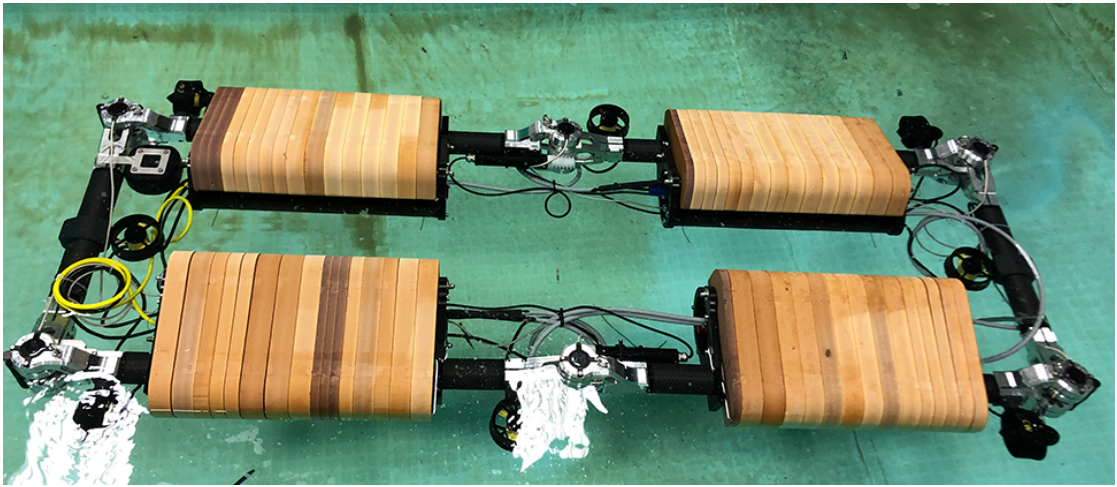


Figure 1.8: RUVIFIST prototype survey configuration

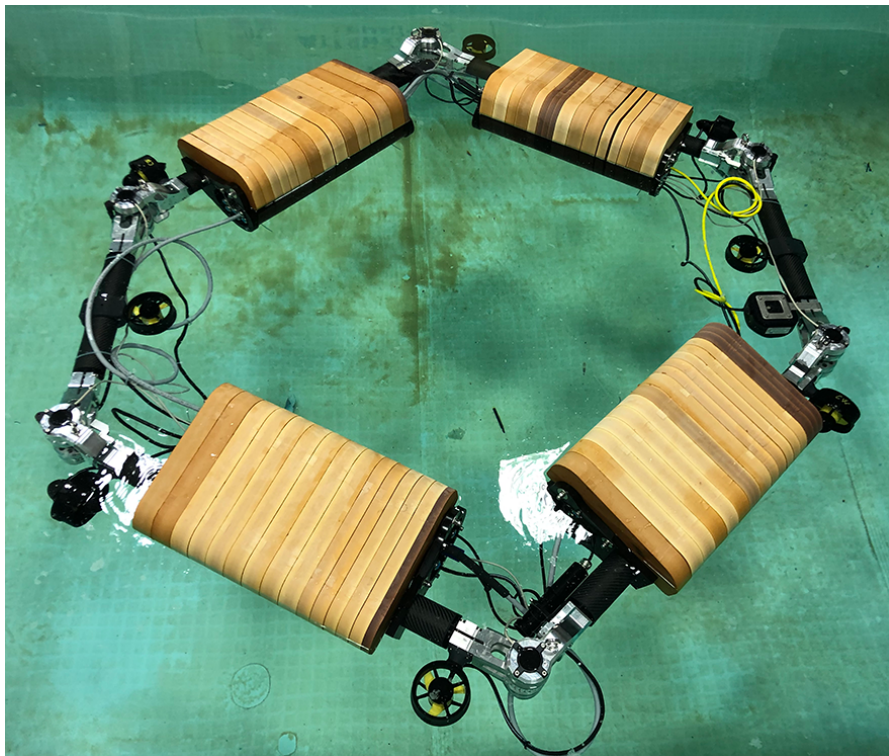


Figure 1.9: RUVIFIST prototype hovering configuration

Part I

Chapter 2

Modelling of the AURV

In this chapter we will derive a model of the RUVIFIST in its “survey” configuration, according to the procedure outlined by Fossen. Being the modelling of rigid bodies moving in a fluid widely studied in literature, please refer to [6] for more details. Since it describes exactly the dynamic behaviour of the AURV to be controlled, this model will be used exclusively for simulation purposes, serving as a virtual experimentation platform. Specifically, it enables testing of the implemented controller as well as potential future ones. This approach helps mitigate the significant costs associated with transporting the AUV to sea for physical testing.

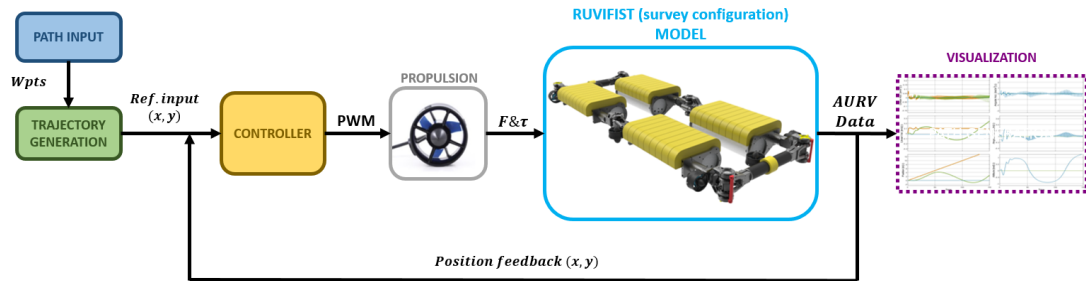


Figure 2.1: Closed-loop AURV model system simulator scheme

With reference to Figure 2.1, the process begins with the generation of a series of waypoints, referred to as the *Path Input*. These waypoints are provided only in terms of X and Y coordinates, defining the desired positions that the RUVIFIST should reach during its operation.

From these waypoints, a trajectory is generated: this trajectory is always two-dimensional, confined to the XY plane, and serves as the input to our model, denoted as the *Trajectory Generation*. The trajectory provides a continuous

reference path for the AURV to follow, ensuring smooth navigation between the predefined waypoints.

The control system, composed of a *Line-of-Sight (LOS)* guidance algorithm and a *Proportional-Integral-Derivative (PID)* controller, plays a crucial role in tracking the trajectory: the controller continuously determines the closest point on the trajectory to the current AURV position, which is obtained through feedback mechanisms. This ensures that the AURV remains on the intended path and corrects deviations in real-time.

Once the controller identifies the nearest point on the trajectory, it generates control signals in the form of *Pulse Width Modulation (PWM)* commands, which are then sent to the propulsion system. Specifically, the PID controller calculates the necessary thrust and torque required to minimize the error between the desired and actual trajectory, signals that then are converted into PWM signals that adjust the thrust levels of the AURV's propulsion system, including thrusters and actuators. The propulsion system translates these PWM signals into physical forces and moments applied to the AURV, allowing it to maneuver accordingly.

Upon receiving the control inputs, the AURV's dynamic and kinematic model processes these forces and moments to determine the vehicle's resulting motion. This model simulates the interactions between the control efforts and the AURV's physical behavior, taking into account hydrodynamic forces, mass properties, and environmental disturbances that will be discussed in the following sections. The computed outputs, labeled as *AURV Data* in the figure, include acceleration, velocity, position, actuation states and the resulting forces and moments acting on the vehicle. These data are visualized in the block referred to as *Visualization*, providing a comprehensive representation of the AURV's behavior, which will be further analyzed in chapter 4.

2.1 Notation

The motion of an underwater AUV in 6 DOF can be represented in a vectorial form using the SNAME notation (Society of Naval Architects and Marine Engineers, 1950), as shown in table 2.1: position and orientation are described by six generalized coordinates, while their time derivatives describe the linear and angular velocities of the vehicle.

According to the SNAME notation, it is possible to refer to the generalized pose, velocity and forces and moments coordinates by (2.1), (2.2) and (2.3) vectors, respectively:

Degree of Freedom	Forces and moments	Linear and angular velocities	Positions and orientation
Surge - motion in the x direction	X	u	x
Sway - motion in the y direction	Y	v	y
Heave - motion in the z direction	Z	w	z
Roll - rotation about the x axis	K	p	ϕ
Pitch - rotation about the y axis	M	q	θ
Yaw - rotation about the z axis	N	r	ψ

Table 2.1: SNAME notation for marine vessels

$$\boldsymbol{\eta} = [x \ y \ z \ \phi \ \theta \ \psi]^T \quad (2.1)$$

$$\boldsymbol{\nu} = [u \ v \ w \ p \ q \ r]^T \quad (2.2)$$

$$\boldsymbol{\tau} = [X \ Y \ Z \ K \ M \ N]^T \quad (2.3)$$

Their sub-vectors are given by using the following vector notations:

- **Position:**

$$\boldsymbol{p} = [x \ y \ z]^T \in \mathbb{R}^3$$

- **Orientation (in Euler angles):**

$$\boldsymbol{\Theta} = [\phi \ \theta \ \psi]^T \in SO(3)$$

- **Linear velocity:**

$$\boldsymbol{v} = [u \ v \ w]^T \in \mathbb{R}^3$$

- **Angular velocity:**

$$\boldsymbol{\omega} = [p \ q \ r]^T \in \mathbb{R}^3$$

- **Force on AUV:**

$$\boldsymbol{f} = [X \ Y \ Z]^T \in \mathbb{R}^3$$

- **Moment on AUV:**

$$\mathbf{m} = \begin{bmatrix} K & M & N \end{bmatrix}^T \in \mathbb{R}^3$$

where:

- \mathbb{R}^3 denotes the three dimensional of Euclidean space
- $SO(3)$ indicates the three dimensional sphere in which three angles are defined on the interval of $[-\pi, \pi]$ for ϕ and ψ , and the interval of $[-\pi/2, \pi/2]$ for θ

Therefore, the general motion of an underwater vehicle in 6 DOF can be described by the following vectors:

$$\boldsymbol{\eta} = \begin{bmatrix} \mathbf{p} \\ \boldsymbol{\Theta} \end{bmatrix} \in \mathbb{R}^3 \times SO(3) \quad (2.4)$$

$$\boldsymbol{\nu} = \begin{bmatrix} \mathbf{v} \\ \boldsymbol{\omega} \end{bmatrix} \in \mathbb{R}^6 \quad (2.5)$$

$$\boldsymbol{\tau} = \begin{bmatrix} \mathbf{f} \\ \mathbf{m} \end{bmatrix} \in \mathbb{R}^6 \quad (2.6)$$

where:

- $\boldsymbol{\eta}$ is the position and orientation (pose) vector
- $\boldsymbol{\nu}$ is the linear and angular velocity screw
- $\boldsymbol{\tau}$ is the force and moment screw

The representation of $\boldsymbol{\nu}$ and $\boldsymbol{\tau}$ in \mathbb{R}^6 is adopted for convenience; however, this is not an exact formulation, as these quantities are screws rather than vectors.

2.2 Equations of motion

The study of RUVIFIST's model can be divided into two parts: kinematics, which treats only geometrical aspects of motion, and dynamics, which is the analysis of the forces causing the motion.

The overall 6 DOF marine craft equation of motion can be written in a vectorial form as follows:

$$\dot{\boldsymbol{\eta}} = \mathbf{J}_{\boldsymbol{\Theta}}(\boldsymbol{\eta})\boldsymbol{\nu} \quad (2.7)$$

$$\mathbf{M}\dot{\boldsymbol{\nu}} + \mathbf{C}(\boldsymbol{\nu})\boldsymbol{\nu} + \mathbf{D}(\boldsymbol{\nu})\boldsymbol{\nu} + \mathbf{g}(\boldsymbol{\eta}) = \boldsymbol{\tau} \quad (2.8)$$

where:

- J_{Θ} is the Jacobian matrix
- M is the sum of the rigid body mass matrix $M_{\text{RB}}^{\text{CG}}$ and the added mass matrix M_A
- $C(\nu)$ is the sum of the rigid body Coriolis and centrifugal contribution $C_{\text{RB}}^{\text{CG}}$ and added mass Coriolis and centrifugal contribution $C_A(\nu)$
- $D(\nu)$ includes all damping effects
- $g(\eta)$ is the hydrostatic term

These terms and their respective properties will be further analyzed in the forthcoming sections.

2.3 Rigid Body's Kinematics

2.3.1 Reference Frames

When analysing the motion of a marine vehicle in 6 DOF, it is convenient to define two reference frames, as shown in [Figure 2.2] and [Figure 2.3]:

NED (North-East-Down frame), with coordinate system $\{n\} = (x_n, y_n, z_n)$ and origin o_n

This is usually defined as the tangent plane on the surface of the Earth, fixed in the vicinity of the vehicle. It is the coordinate system we refer to in our everyday life, with the x axis pointing towards the true North, the y axis pointing towards East and the z axis pointing downwards normal to the Earth surface.

BODY (Body-fixed frame), with coordinate system $\{b\} = (x_b, y_b, z_b)$ and origin o_b

This is a moving frame that is fixed to the vehicle. Position and orientation of the craft are usually described relative to the inertial frame, $\{n\}$ for the marine case, while linear and angular velocities are usually expressed in the body-fixed frame. The axes are chosen to coincide with the principal axes of inertia of the vehicle and are called longitudinal, transversal and normal axis, respectively the x , y , and z axes.

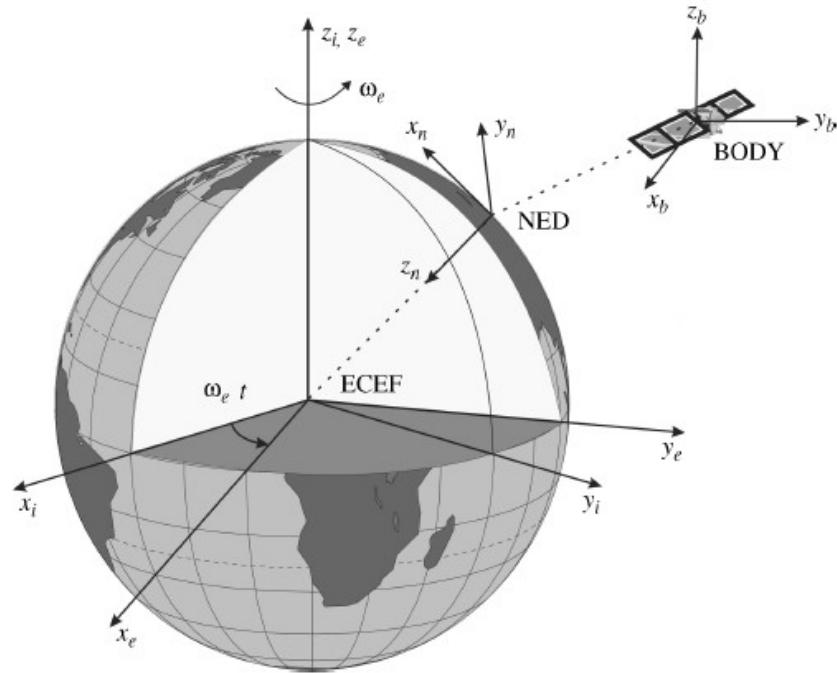


Figure 2.2: Reference frames

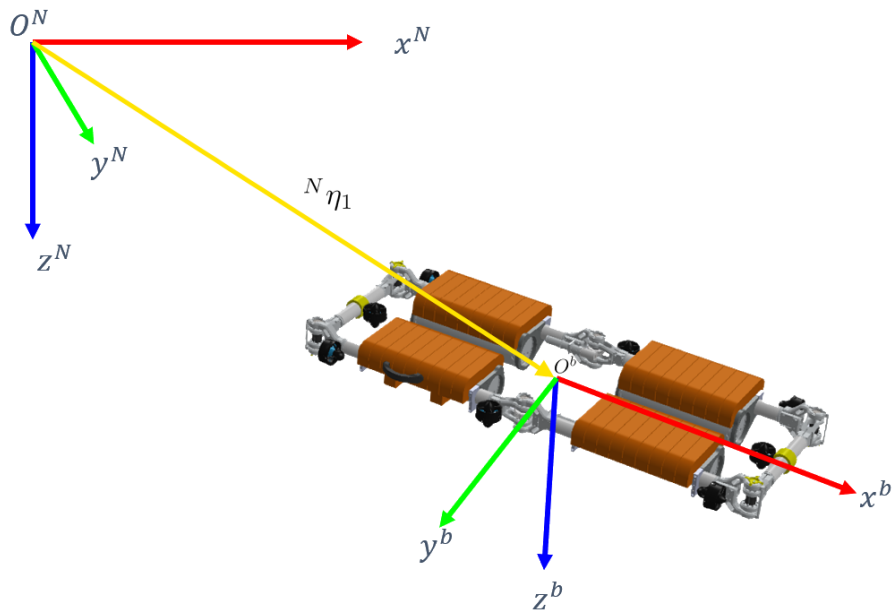


Figure 2.3: NED and BODY frames of RUVIFIST

2.3.2 Transformation Between BODY and NED

It is possible to describe the orientation of the AUV with different representations, such as Euler angles and quaternions. Euler angles are known to suffer from singularities, commonly referred to as *gimbal lock*, where the representation becomes ambiguous and loses a degree of freedom. Quaternions, being four-dimensional, do not have this issue and can represent all orientations without singular points. For this reason, in this work the quaternion kinematics model will be used.

Quaternion Transformation

According to the study of quaternion kinematics (Chou - 1992) [7], a quaternion q is defined as a complex number formed by four units:

$$\mathbf{q} = [\eta \ \epsilon_1 \ \epsilon_2 \ \epsilon_3]^T \quad (2.9)$$

where q_0 is a real parameter and the other three units are imaginary parameters. It is possible to compute these parameters using a rotation θ around a unit vector $u = [u_1 \ u_2 \ u_3]^T$ (i.e. $|\mathbf{u}| = 1$) in the following way:

- Real part

$$\eta = \cos \frac{\theta}{2} \quad (2.10)$$

- Imaginary part

$$\begin{bmatrix} \epsilon_1 \\ \epsilon_2 \\ \epsilon_3 \end{bmatrix} = \begin{bmatrix} u_1 \sin \frac{\theta}{2} \\ u_2 \sin \frac{\theta}{2} \\ u_3 \sin \frac{\theta}{2} \end{bmatrix} \quad (2.11)$$

As a consequence, the quaternion can be represented by the following structure:

$$q = \begin{bmatrix} \eta \\ \epsilon_1 \\ \epsilon_2 \\ \epsilon_3 \end{bmatrix} = \begin{bmatrix} \cos \frac{\theta}{2} \\ u_1 \sin \frac{\theta}{2} \\ u_2 \sin \frac{\theta}{2} \\ u_3 \sin \frac{\theta}{2} \end{bmatrix} = \begin{bmatrix} \cos \frac{\theta}{2} \\ \mathbf{u} \sin \frac{\theta}{2} \end{bmatrix} \quad (2.12)$$

Since the unit quaternion satisfies $\mathbf{q}^T \mathbf{q} = 1$, the transformation between the linear velocity expressed in body frame and the linear velocity expressed in NED frame results:

$$\dot{\mathbf{p}} = \mathbf{R}_b^n(\mathbf{q}) \mathbf{v}^b \quad (2.13)$$

where

$$\mathbf{R}_b^n(\mathbf{q}) = \begin{bmatrix} 1 - 2(\varepsilon_2^2 + \varepsilon_3^2) & 2(\varepsilon_1\varepsilon_2 - \varepsilon_3\eta) & 2(\varepsilon_1\varepsilon_3 - \varepsilon_2\eta) \\ 2(\varepsilon_1\varepsilon_2 - \varepsilon_3\eta) & 1 - 2(\varepsilon_1^2 + \varepsilon_3^2) & 2(\varepsilon_2\varepsilon_3 - \varepsilon_1\eta) \\ 2(\varepsilon_1\varepsilon_3 - \varepsilon_2\eta) & 2(\varepsilon_2\varepsilon_3 - \varepsilon_1\eta) & 1 - 2(\varepsilon_1^2 + \varepsilon_2^2) \end{bmatrix} \quad (2.14)$$

while the transformation matrix between the angular velocity expressed in body frame and the time derivative of the unit quaternion is given by:

$$\dot{\mathbf{q}} = \mathbf{T}_q(\mathbf{q})\mathbf{w}^b \quad (2.15)$$

where

$$\mathbf{T}_q(\mathbf{q}) = \begin{bmatrix} -\varepsilon_1 & -\varepsilon_2 & -\varepsilon_3 \\ \eta & -\varepsilon_3 & \varepsilon_2 \\ \varepsilon_3 & \eta & -\varepsilon_1 \\ -\varepsilon_2 & \varepsilon_1 & \eta \end{bmatrix}. \quad (2.16)$$

It is useful to collect the kinematic equations in 6-dimensional matrix forms. Recalling equations (2.4), (2.5), (2.13) and (2.15) we can thus write (2.7) as:

$$\dot{\boldsymbol{\xi}} = \mathbf{J}(\mathbf{q})\boldsymbol{\nu} \iff \begin{bmatrix} \dot{\mathbf{p}} \\ \dot{\mathbf{q}} \end{bmatrix} = \begin{bmatrix} \mathbf{R}_b^n(\mathbf{q}) & \mathbf{0}_{3 \times 3} \\ \mathbf{0}_{4 \times 3} & \mathbf{T}_q(\mathbf{q}) \end{bmatrix} \begin{bmatrix} \mathbf{v}^b \\ \boldsymbol{\omega}^b \end{bmatrix} \quad (2.17)$$

2.4 Rigid Body's Dynamics

We now begin analyzing the terms of formula (2.8). In this section we focus specifically on rigid-body dynamics, expressed as follows:

$$\mathbf{M}_{RB}\dot{\boldsymbol{\nu}} + \mathbf{C}_{RB}(\boldsymbol{\nu})\boldsymbol{\nu} = \boldsymbol{\tau}_{RB} \quad (2.18)$$

where:

- \mathbf{M}_{RB} is the rigid-body mass matrix
- \mathbf{C}_{RB} is the rigid-body Coriolis and centripetal matrix due to the rotation of $\{b\}$ about the inertial frame $\{n\}$
- $\boldsymbol{\nu} = [u, v, w, p, q, r]^T$ is the generalized velocity vector expressed in $\{b\}$
- $\boldsymbol{\tau}_{RB} = [X, Y, Z, K, M, N]^T$ is a generalized vector of external forces and moments expressed in $\{b\}$

The rigid-body equation of motion are derived using the *Newton-Euler* formulation and are usually represented in two Body-fixed reference points: the origin o_n of $\{b\}$, CO (i.e., the geometric center) and the center of gravity, CG (i.e., the center

of mass).

In the study of rigid-body dynamics, computations are initially performed around the center of gravity CG, due to its simplicity in deriving translational motion equations and defining the inertia matrix; once the motion equations are established, they are then transformed to the geometric center CO, which is often chosen in marine craft to facilitate more effective control system design and optimize performance.

$$\begin{aligned}
 \mathbf{M}_{RB}^{CO} &= \begin{bmatrix} m\mathbf{1}_{3 \times 3} & -m\mathbf{S}(\mathbf{p}_C^b) \\ m\mathbf{S}(\mathbf{p}_C^b) & \mathbf{I}_o \end{bmatrix} \\
 &= \begin{bmatrix} m & 0 & 0 & 0 & mz_C & -my_C \\ 0 & m & 0 & -mz_C & 0 & mx_C \\ 0 & 0 & m & my_C & -mx_C & 0 \\ 0 & -mz_C & my_C & I_x & -I_{xy} & -I_{xz} \\ mz_C & 0 & -mx_C & -I_{yx} & I_y & -I_{yz} \\ -my_C & mx_C & 0 & -I_{zx} & -I_{zy} & I_z \end{bmatrix} \quad (2.19)
 \end{aligned}$$

$$\mathbf{C}_{RB}^{CO} = \begin{bmatrix} m\mathbf{S}(\boldsymbol{\omega}^b) & -m\mathbf{S}(\boldsymbol{\omega}^b)\mathbf{S}(\mathbf{p}_C^b) \\ m\mathbf{S}(\mathbf{p}_C^b)\mathbf{S}(\boldsymbol{\omega}^b) & -\mathbf{S}(\mathbf{I}_o\boldsymbol{\omega}^b) \end{bmatrix} \quad (2.20)$$

For more information about the computations, please refer to appendix A.

2.5 Hydrostatics

When submerged in a fluid, a rigid body is under the effect of both the gravitational force and the buoyancy [Figure 2.4].

Buoyancy is not a function of a relative movement between body and fluid, thus it is considered as an hydrostatic effect, expressed by the term $\mathbf{g}_{RB}(\mathbf{q})$, with reference to formula (2.8).

Let's consider the acceleration of gravity $\mathbf{g}^n = \begin{bmatrix} 0 \\ 0 \\ 9.81 \end{bmatrix} m/s^2$, the volume of the body Δ and its mass m . The submerged weight of the body is defined as:

$$W = m\|\mathbf{g}^n\| \quad (2.21)$$

while its buoyancy, considering the water density ρ_w , is defined as:

$$B = \rho_w\Delta\|\mathbf{g}^n\| \quad (2.22)$$

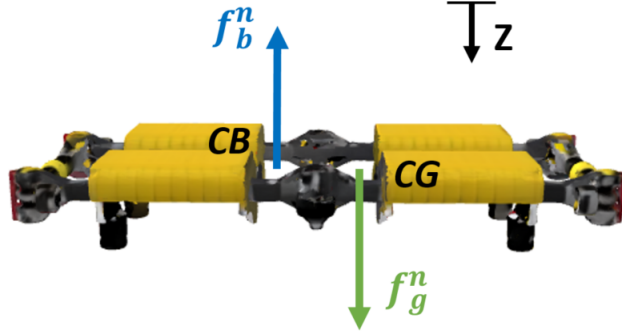


Figure 2.4: Gravitational and buoyancy forces acting on the center of gravity CG and on the center of buoyancy CB of RUVIFIST

The gravity force, acting in the center of mass $\mathbf{p}_C^b = [x_C \ y_C \ z_C]^T$ is represented in Body-fixed frame by:

$$\mathbf{f}_G^b(\mathbf{R}_n^b) = \mathbf{R}_n^b \begin{bmatrix} 0 \\ 0 \\ W \end{bmatrix} \quad (2.23)$$

while the buoyancy force, acting in the center of buoyancy $\mathbf{p}_B^b = [x_B \ y_B \ z_B]^T$ is represented in Body-fixed frame by:

$$\mathbf{f}_B^b(\mathbf{R}_n^b) = -\mathbf{R}_n^b \begin{bmatrix} 0 \\ 0 \\ B \end{bmatrix} \quad (2.24)$$

The (6×1) vector of forces and moments due to gravity and buoyancy in the Body-fixed frame is represented by:

$$\mathbf{g}_{RB}(\mathbf{R}_n^b) = - \begin{bmatrix} \mathbf{f}_G^b(\mathbf{R}_n^b) + \mathbf{f}_B^b(\mathbf{R}_n^b) \\ \mathbf{p}_C^b \times \mathbf{f}_G^b(\mathbf{R}_n^b) + \mathbf{p}_B^b \times \mathbf{f}_B^b(\mathbf{R}_n^b) \end{bmatrix} \quad (2.25)$$

In terms of quaternions, it is represented by:

$$\mathbf{g}(\mathbf{q}) = \begin{bmatrix} 2(\varepsilon_2\eta - \varepsilon_1\varepsilon_3)(W - B) \\ -2(\varepsilon_1\eta + \varepsilon_2\varepsilon_3)(W - B) \\ (-\eta^2 + \varepsilon_1^2 + \varepsilon_2^2 - \varepsilon_3^2)(W - B) \\ (-\eta^2 + \varepsilon_1^2 + \varepsilon_2^2 - \varepsilon_3^2)(y_C W - y_B B) + 2(\varepsilon_1\eta + \varepsilon_2\varepsilon_3)(z_C W - z_B B) \\ -(-\eta^2 + \varepsilon_1^2 + \varepsilon_2^2 - \varepsilon_3^2)(x_C W - x_B B) + 2(\varepsilon_2\eta - \varepsilon_1\varepsilon_3)(z_C W - z_B B) \\ -2(\varepsilon_1\eta + \varepsilon_2\varepsilon_3)(x_C W - x_B B) - 2(\varepsilon_2\eta - \varepsilon_1\varepsilon_3)(y_C W - y_B B) \end{bmatrix} \quad (2.26)$$

Buoyancy and maneuverability

The relationship between buoyancy and maneuverability plays a key role in the design of underwater vehicles.

A neutrally buoyant underwater vehicle will satisfy $W = B$.

It is convenient to design underwater vehicles with $B > W$ (positive buoyancy) such that the vehicle will surface automatically in emergency situations, such as power failure.

The buoyancy magnitude B should be slightly greater than W : if the vehicle is designed such that $B \gg W$, too much control energy is required to keep the vehicle submerged.

2.6 Hydrodynamics

In this section we will discuss the main hydrodynamic effects involved in our dynamical system. In particular, the following terms of formula (2.8) will be analyzed: the added mass and inertia, $\mathbf{M}_A \dot{\boldsymbol{\nu}}$ and $\mathbf{C}_A(\boldsymbol{\nu})$, and the damping effect, $D_{RB}(\boldsymbol{\nu})$.

It is essential to note that in fluid dynamics it is difficult to develop a reliable model for most of the hydrodynamic effects. A rigorous analysis for incompressible fluids would need to resort to the Navier-Stokes equations. For more details please refer to [6], [8] and [9].

2.6.1 Added Mass and Inertia

When a rigid body is moving through a fluid, the surrounding fluid's inertia is influenced by the motion of the body, leading to an acceleration of the adjacent fluid mass.

The additional inertia of the fluid surrounding the body is accelerated by the movement of the body. In industrial robotics, this presence has no effect, since the density of the air is much smaller than the density of a moving mechanical system. However, in underwater applications, where the density of water $\rho \simeq 1000 \text{kg/m}^3$ is comparable to that of the vehicle, this effect becomes substantial and directly impacts the moving body.

As the body moves, the surrounding fluid is accelerated along with it, requiring an external force to sustain this acceleration. In response, the fluid exerts an equal and opposite reaction force on the body. This reaction force is known as the added mass effect.

It is important to note that the added mass does not represent a physical mass of

fluid being incorporated into the system. Instead, as the marine craft moves, it induces motion in the otherwise stationary fluid. The fluid must displace to allow the craft to pass and subsequently close in behind it [Figure 2.5]. As a consequence, the fluid acquires kinetic energy that it would not possess otherwise.

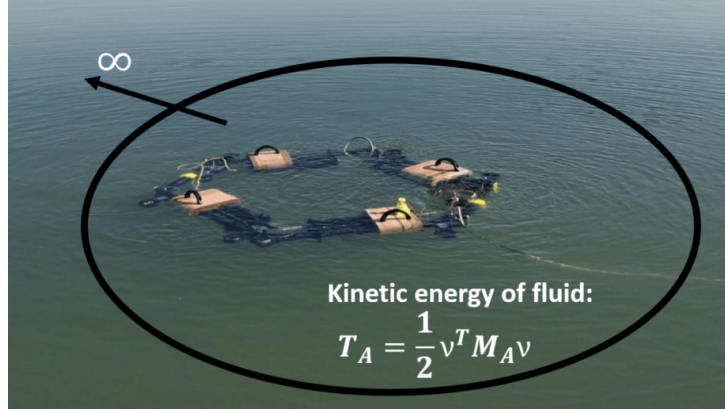


Figure 2.5: Rigid-body and fluid kinetic energy

The expression for the fluid kinetic energy T_A is written as a quadratic form (Lamb, 1932):

$$T_A = \frac{1}{2} \boldsymbol{\nu}^T \mathbf{M}_A \boldsymbol{\nu}, \quad \dot{\mathbf{M}}_A = 0 \quad (2.27)$$

where $\mathbf{M}_A = \mathbf{M}_A^T \geq 0$ is the 6×6 *system inertia matrix* of added mass terms:

$$\mathbf{M}_A = - \begin{bmatrix} X_{\dot{u}} & X_{\dot{v}} & X_{\dot{w}} & X_{\dot{p}} & X_{\dot{q}} & X_{\dot{r}} \\ Y_{\dot{u}} & Y_{\dot{v}} & Y_{\dot{w}} & Y_{\dot{p}} & Y_{\dot{q}} & Y_{\dot{r}} \\ Z_{\dot{u}} & Z_{\dot{v}} & Z_{\dot{w}} & Z_{\dot{p}} & Z_{\dot{q}} & Z_{\dot{r}} \\ K_{\dot{u}} & K_{\dot{v}} & K_{\dot{w}} & K_{\dot{p}} & K_{\dot{q}} & K_{\dot{r}} \\ M_{\dot{u}} & M_{\dot{v}} & M_{\dot{w}} & M_{\dot{p}} & M_{\dot{q}} & M_{\dot{r}} \\ N_{\dot{u}} & N_{\dot{v}} & N_{\dot{w}} & N_{\dot{p}} & N_{\dot{q}} & N_{\dot{r}} \end{bmatrix} \quad (2.28)$$

The notation of SNAME (1950) for the hydrodynamic derivatives is used in this expression.

The added mass has also an added Coriolis and centripetal contribution. It can be demonstrated that the matrix expression can always be parameterized such that:

$$\mathbf{C}_A(\boldsymbol{\nu}) = \begin{bmatrix} 0 & 0 & 0 & 0 & -a_3 & a_2 \\ 0 & 0 & 0 & a_3 & 0 & -a_1 \\ 0 & 0 & 0 & -a_2 & a_1 & 0 \\ 0 & -a_3 & a_2 & 0 & -b_3 & b_2 \\ a_3 & 0 & -a_1 & b_3 & 0 & -b_1 \\ -a_2 & a_1 & 0 & -b_2 & b_1 & 0 \end{bmatrix} \quad (2.29)$$

where:

$$\begin{aligned} a_1 &= X_{\dot{u}}u + X_{\dot{v}}v + X_{\dot{w}}w + X_{\dot{p}}p + X_{\dot{q}}q + X_{\dot{r}}r \\ a_2 &= Y_{\dot{u}}u + Y_{\dot{v}}v + Y_{\dot{w}}w + Y_{\dot{p}}p + Y_{\dot{q}}q + Y_{\dot{r}}r \\ a_3 &= Z_{\dot{u}}u + Z_{\dot{v}}v + Z_{\dot{w}}w + Z_{\dot{p}}p + Z_{\dot{q}}q + Z_{\dot{r}}r \\ b_1 &= K_{\dot{u}}u + K_{\dot{v}}v + K_{\dot{w}}w + K_{\dot{p}}p + K_{\dot{q}}q + K_{\dot{r}}r \\ b_2 &= M_{\dot{u}}u + M_{\dot{v}}v + M_{\dot{w}}w + M_{\dot{p}}p + M_{\dot{q}}q + M_{\dot{r}}r \\ b_3 &= N_{\dot{u}}u + N_{\dot{v}}v + N_{\dot{w}}w + N_{\dot{p}}p + N_{\dot{q}}q + N_{\dot{r}}r \end{aligned}$$

In general, the motion of an underwater vehicle moving in 6 DOF at high speed exhibits significant non-linearity and coupling; however, in many applications the vehicle's movement is restricted to low speed. In addition, if the vehicle has three planes of symmetry, it implies that the contribution from the off-diagonal elements in the matrix \mathbf{M}_A can be neglected.

It is thus possible to simplify the equations (2.28) and (2.29) as follows:

$$\mathbf{M}_A = \mathbf{M}_A^T = -diag \{X_{\dot{u}}, Y_{\dot{v}}, Z_{\dot{w}}, K_{\dot{p}}, M_{\dot{q}}, N_{\dot{r}}\} \quad (2.30)$$

$$\mathbf{C}_A(\boldsymbol{\nu}) = \mathbf{C}_A^T(\boldsymbol{\nu}) = \begin{bmatrix} 0 & 0 & 0 & 0 & -Z_{\dot{w}}w & Y_{\dot{v}}v \\ 0 & 0 & 0 & Z_{\dot{w}}w & 0 & -X_{\dot{u}}u \\ 0 & 0 & 0 & -Y_{\dot{v}}v & X_{\dot{u}}u & 0 \\ 0 & -Z_{\dot{w}}w & Y_{\dot{v}}v & 0 & -N_{\dot{r}}r & M_{\dot{q}}q \\ Z_{\dot{w}}w & 0 & -X_{\dot{u}}u & N_{\dot{r}}r & 0 & -K_{\dot{p}}p \\ -Y_{\dot{v}}v & X_{\dot{u}}u & 0 & -M_{\dot{q}}q & K_{\dot{p}}p & 0 \end{bmatrix} \quad (2.31)$$

2.6.2 Damping Effects

The damping effects are related to the presence of fluid viscosity that leads to the generation of dissipative drag and lift forces acting on the body.

A common simplification is to consider only linear and quadratic damping terms and group these terms in a matrix \mathbf{D}_{RB} such that $\mathbf{D}_{RB}(\boldsymbol{\nu}) > \mathbf{0}$, $\forall \boldsymbol{\nu} \in \mathbb{R}^6$.

$$\begin{aligned} \mathbf{D}_{RB}(\boldsymbol{\nu}) &= -diag\{X_u, Y_v, Z_w, K_p, M_q, N_r\} + \\ &\quad - diag\{X_{u|u}|u|, Y_{v|v}|v|, Z_{w|w}|w|, K_{p|p}|p|, M_{q|q}|q|, N_{r|r}|r|\} \end{aligned} \quad (2.32)$$

The following observations can be made:

- The coefficients of this matrix are considered to be constant
- Assuming a diagonal structure for the damping matrix implies neglecting the coupling dissipative terms

The viscous effects can be considered as the sum of two forces, the *drag* and the *lift* forces. The former are parallel to the relative velocity between the body and the fluid, while the latter are normal to it. Both drag and lift forces are supposed to act on the center of mass of the body.

Considering the rigid body as a sphere moving in a fluid, the drag force can be modeled as:

$$F_{drag} = \frac{1}{2}\rho_w U^2 S C_d (R_n), \quad (2.33)$$

where:

- ρ_w is the fluid density
- U is the velocity of the sphere
- C_d is the drag coefficient
- S is the frontal area of the sphere
- R_n is the Reynolds number

The lift forces can be represented as:

$$F_{lift} = \frac{1}{2}\rho_w U^2 S C_l (R_n, \alpha), \quad (2.34)$$

where:

- ρ_w is the fluid density
- U is the velocity of the sphere
- C_l is the lift coefficient, depending on the angle of attack α
- S is the frontal area of the sphere
- R_n is the Reynolds number

2.7 Ocean Current Forces and Moments

The control of marine vehicles must consider environmental disturbances like waves, wind, and ocean currents, which significantly impact motion dynamics, especially in shallow waters. Understanding these forces is crucial for ensuring precise navigation and stability in marine vehicle operations.

In this section, we will focus on the effect of ocean currents, as they play a dominant role in long-term vehicle drift, energy consumption, and maneuverability, making their impact particularly critical for autonomous marine systems [10] [11].

The influence of ocean currents on a marine craft can be accounted for by modifying the generalized velocity vector in the hydrodynamic terms to reflect relative velocity ν_r :

$$\nu_r = \nu - \nu_c \quad (2.35)$$

where $\nu_c \in \mathbb{R}^6$ represents the velocity of the ocean current expressed in the Body-fixed frame.

Definition: irrotational fluid

In the case of an irrotational fluid, the generalized ocean current velocity is given by:

$$\nu_c = [u_c \ v_c \ w_c \ 0 \ 0 \ 0]^T \quad (2.36)$$

where $v_c^b = [u_c \ v_c \ w_c]^T$ represents the linear velocity component.

The relationship between the ocean current linear velocity vector in the NED and Body-fixed frames is expressed as:

$$v_c^n = R_b^n(\Theta_{nb})v_c^b \quad (2.37)$$

where $\Theta_{nb} = [\phi \ \theta \ \psi]^T$ represents the Euler angles defining the transformation between the BODY and NED frames and $R_b^n(\Theta_{nb}) \in SO(3)$ is the associated rotation matrix.

Definition: irrotational constant ocean current

For an irrotational constant ocean current in the NED frame, the following conditions must hold:

$$\dot{v}_c^n = \dot{R}_b^n(\Theta_{nb})v_c^b + R_b^n(\Theta_{nb})\dot{v}_c^b = 0 \quad (2.38)$$

2.7.1 Equation of motion including Ocean Currents

In order to effectively model the influence of irrotational ocean currents on marine craft dynamics, the equation (2.8) is formulated as follows:

$$M_{RB}\dot{\nu} + C_{RB}(\nu)\nu + g(q) + M_A\dot{\nu}_r + C_A(\nu_r)\nu_r + D(\nu_r)\nu_r = \tau \quad (2.39)$$

where the relative velocity vector is defined as:

$$\nu_r = \begin{bmatrix} v^b - v_c^b \\ \omega_{b/n}^b \end{bmatrix} \quad (2.40)$$

It is important to note that the rigid-body dynamics remain unaffected by ocean currents.

Theorem: Coriolis and Centripetal matrix property

If the Coriolis and centripetal matrix $C_{RB}(\nu_r)$ is independent of the linear velocity $\nu_l = [u \ v \ w]^T$, and the ocean current is irrotational and constant, then the rigid-body dynamics satisfy (Hegrenaes, 2010):

$$M_{RB}\dot{\nu} + C_{RB}(\nu)\nu \equiv M_{RB}\dot{\nu}_r + C_{RB}(\nu_r)\nu_r \quad (2.41)$$

Since the Coriolis and centripetal matrix is independent of the linear velocity ν_l , it follows that:

$$C_{RB}(\nu_r) = C_{RB}(\nu) \quad (2.42)$$

Additionally, the property:

$$M_{RB}\dot{\nu}_c + C_{RB}(\nu_r)\nu_c = 0 \quad (2.43)$$

is established by expanding the matrices M_{RB} and $C_{RB}(\nu_r)$ along with their respective acceleration and velocity vectors:

$$\begin{bmatrix} mI_{3 \times 3} & -mS(r_g^b) \\ mS(r_g^b) & I_b \end{bmatrix} \begin{bmatrix} -S(\omega_{b/n}^b)v_c^b \\ 0_{3 \times 1} \end{bmatrix} + \begin{bmatrix} mS(\omega_{b/n}^b) & -mS(r_g^b)S(\omega_{b/n}^b) \\ mS(r_g^b)S(\omega_{b/n}^b) & S(I_b\omega_{b/n}^b) \end{bmatrix} \begin{bmatrix} v_c^b \\ 0_{3 \times 1} \end{bmatrix} = 0 \quad (2.44)$$

Finally, it follows that:

$$M_{RB}\dot{\nu} + C_{RB}(\nu)\nu = M_{RB}(\dot{\nu}_r + \dot{\nu}_c) + C_{RB}(\nu_r)(\nu_r + \nu_c) = M_{RB}\dot{\nu}_r + C_{RB}(\nu_r)\nu_r \quad (2.45)$$

Applying this theorem to the equations of motion (2.7) and (2.8), we obtain the following differential equations:

$$\dot{\xi} = J(q)\nu_r + \begin{bmatrix} v_c^n \\ 0 \end{bmatrix} \quad (2.46)$$

$$M\dot{\nu}_r + C(\nu_r)\nu_r + D(\nu_r)\nu_r + g(q) = \tau \quad (2.47)$$

where $M = M_{RB} + M_A$ and $C(\nu_r) = C_{RB}(\nu_r) + C_A(\nu_r)$.

It is important to note that in formula (2.47) only ν_r is used instead of ν . This model incorporates the bias $\dot{v}_c^n = 0$ at the kinematic level, whereas the model of formula (2.39) accounts for ocean current drift at the dynamic level using $\nu_r = \nu - \nu_c$.

2.8 Dynamic parameters of the system

For simulation purposes, the high fidelity model discussed in section 2.1 was implemented in *MATLAB Simulink* to test the dynamic behaviour of RUVIFIST. In order to do this, the numerical values for all the system parameters discussed before are needed.

All the parameters, along with their corresponding values and units of measurement, are listed in table 3.1. These parameters were previously estimated by the *MdM Lab* team, so for more details on how they were obtained, please refer to [12].

2.8.1 Thruster dynamics and Control allocation

Since RUVIFIST has 8 thrusters, the thruster forces can be represented using the following vector:

$$\mathbf{F} = [F_1 \ F_2 \ F_3 \ F_4 \ F_5 \ F_6 \ F_7 \ F_8]^T \quad (2.48)$$

while the control inputs can be represented using the following one:

$$\mathbf{u} = [u_1 \ u_2 \ u_3 \ u_4 \ u_5 \ u_6 \ u_7 \ u_8]^T \quad (2.49)$$

Given the force vector $\mathbf{f} = [F_x \ F_y \ F_z]^T$ and the moment arms $\mathbf{r} = [l_x \ l_y \ l_z]^T$, the forces and moments in 6 DOF can be determined by:

Symbol	Description	Value
m	mass	90.00 kg
W	weight	882.90 N
B	buoyancy	895.10 N
I_x	moment of inertia	3.85 kg m ²
I_y	moment of inertia	20.95 kg m ²
I_z	moment of inertia	23.51 kg m ²
I_{xy}	products of inertia	0.00 kg m ²
I_{xz}	products of inertia	0.00 kg m ²
I_{yz}	products of inertia	0.00 kg m ²
$ X_{\dot{u}} $	added mass	0.50 kg
$ Y_{\dot{v}} $	added mass	0.50 kg
$ Z_{\dot{w}} $	added mass	0.50 kg
$ K_{\dot{p}} $	added mass	0.50 kg m ² rad ⁻¹
$ M_{\dot{q}} $	added mass	0.50 kg m ² rad ⁻¹
$ N_{\dot{r}} $	added mass	0.50 kg m ² rad ⁻¹
$ X_u $	linear damping	13.10 N s m ⁻¹
$ Y_v $	linear damping	24.60 N s m ⁻¹
$ Z_w $	linear damping	653.80 N s m ⁻¹
$ K_p $	linear damping	55.30 N s rad ⁻¹
$ M_q $	linear damping	418.40 N s rad ⁻¹
$ N_r $	linear damping	29.40 N s rad ⁻¹
$ X_{u u} $	quadratic damping	130.76 N s ² m ⁻²
$ Y_{v v} $	quadratic damping	245.90 N s ² m ⁻²
$ Z_{w w} $	quadratic damping	6537.90 N s ² m ⁻²
$ K_{p p} $	quadratic damping	553.30 N s ² rad ⁻²
$ M_{q q} $	quadratic damping	4184.20 N s ² rad ⁻²
$ N_{r r} $	quadratic damping	294.20 N s ² rad ⁻²
\mathbf{p}_B^C	coordinates of the CoB	[0.00; 0.00; 0.00] m
\mathbf{p}_C^C	coordinates of the CoM	[0.00; 0.00; 0.00] m

Table 2.2: RUVIFIST's parameters

$$\boldsymbol{\tau} = \begin{bmatrix} \mathbf{f} \\ \mathbf{r} \times \mathbf{f} \end{bmatrix} = \begin{bmatrix} F_x \\ F_y \\ F_z \\ F_z l_y - F_y l_z \\ F_x l_z - F_z l_x \\ F_y l_x - F_x l_y \end{bmatrix} \quad (2.50)$$

Hence, the generalised forces and moments in 6 DOF $\boldsymbol{\tau} \in \mathbb{R}^6$ due to 8 thrusters $\mathbf{F} \in \mathbb{R}^8$ can be then modelled as:

$$\boldsymbol{\tau} = \mathbf{T}(\boldsymbol{\alpha})\mathbf{F} \quad (2.51)$$

where $\mathbf{T} = [\mathbf{t}_1 \ \mathbf{t}_2 \ \mathbf{t}_3 \ \mathbf{t}_4 \ \mathbf{t}_5 \ \mathbf{t}_6 \ \mathbf{t}_7 \ \mathbf{t}_8]^T \in \mathbb{R}^{6 \times 8}$ is the thrust configuration matrix and $\boldsymbol{\alpha} \in \mathbb{R}^8$ is the thrust rotation angle vector.

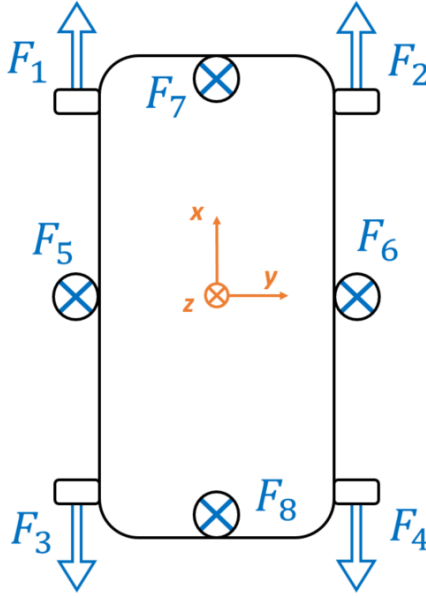


Figure 2.6: RUVIFIST schematic of thrust forces w.r.t. CG

Considering the schematics of [Figure 3.1], the thrust configuration matrix T for RUVIFIST is given by:

$$\mathbf{T} = \begin{bmatrix} 1.0 & 1.0 & -1.0 & -1.0 & 0.0 & 0.0 & 0.0 & 0.0 \\ 0.0 & 0.0 & 0.0 & 0.0 & 0.0 & 0.0 & 0.0 & 0.0 \\ 0.0 & 0.0 & 0.0 & 0.0 & 1.0 & 1.0 & 1.0 & 1.0 \\ 0.0 & 0.0 & 0.0 & 0.0 & -0.3 & 0.3 & 0.0 & 0.0 \\ 0.0 & 0.0 & 0.0 & 0.0 & 0.0 & 0.0 & -0.8 & 0.8 \\ 0.4 & -0.4 & 0.4 & -0.4 & 0.0 & 0.0 & 0.0 & 0.0 \end{bmatrix} \quad (2.52)$$

The control allocation problem computes the control input signal \mathbf{u} to apply to the thrusters such that the overall desired control forces $\boldsymbol{\tau}$ can be generalised. First of all, we need to find a relationship between the input signal \mathbf{u} and the thrust forces \mathbf{F} . Since RUVIFIST uses *BlueRobotics T200 Thrusters* both for the horizontal and vertical thrusts, it is possible to exploit the following relationship shown in [Figure 2.7]:

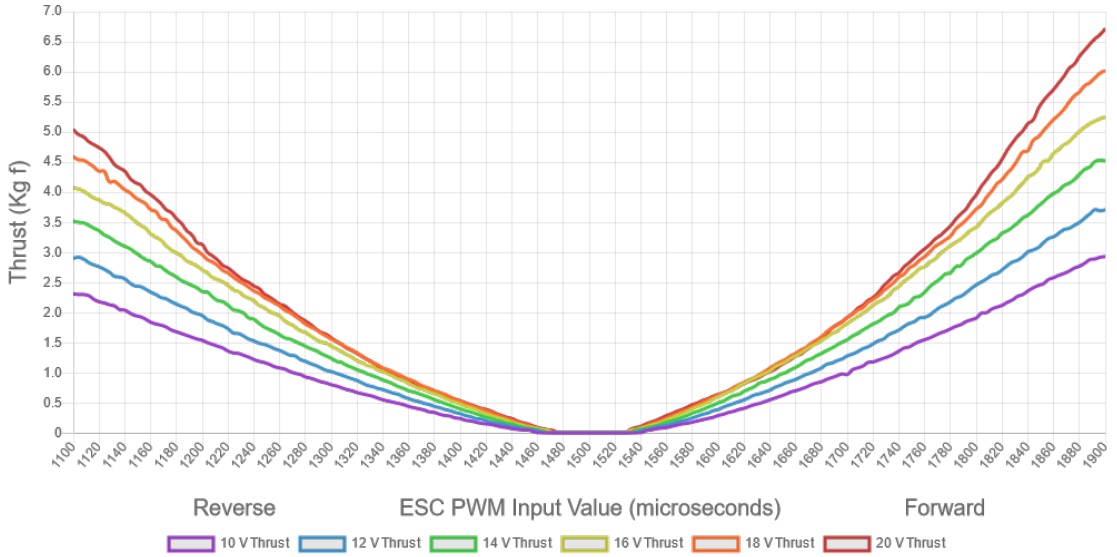


Figure 2.7: T200 BlueRobotics Thrust (kgf) w.r.t. the ESC PWM Input Value (μs)

For more information about the *BlueRobotics T200 Thrusters*, please refer to [13].

We can now derive the inverse of equation (2.51) as:

$$\mathbf{F} = \mathbf{T}^{-1}\boldsymbol{\tau} \quad (2.53)$$

However, since the thrust configuration matrix \mathbf{T} for RUVIFIST is non-square, the *Moore-Penrose pseudo-inverse* \mathbf{T}^+ is applied given by:

$$\mathbf{T}^+ = \mathbf{T}^T (\mathbf{T}\mathbf{T}^T)^{-1} \quad (2.54)$$

Hence, the thrust forces vector \mathbf{F} can be calculated as:

$$\mathbf{F} = \mathbf{T}^+ \boldsymbol{\tau} \quad (2.55)$$

In this way we can give as input the forces and moments vector $\boldsymbol{\tau}$ and get as output the relative thrust forces vector \mathbf{F} . Finally, we can apply to each motor a PWM signal as shown in Figure 2.7 depending on the value of \mathbf{F} .

Chapter 3

Trajectory Tracking

Trajectory tracking is a control approach that ensures a system, such as a robot, vehicle, or marine craft, follows a predefined path while meeting both spatial and temporal constraints. This means the system must reach specific positions at precise times, requiring a guidance mechanism that generates both heading and velocity reference trajectories.

One widely used method for heading control, particularly in marine applications, is the *Line of Sight* (LOS) guidance law. LOS guidance is effective in generating smooth reference trajectories, improving stability, and compensating for disturbances.

Control algorithms like PID controllers, *Model Predictive Control* (MPC), or adaptive methods work alongside LOS guidance to continuously adjust the system's movement based on real-time sensor feedback [Figure 3.1].

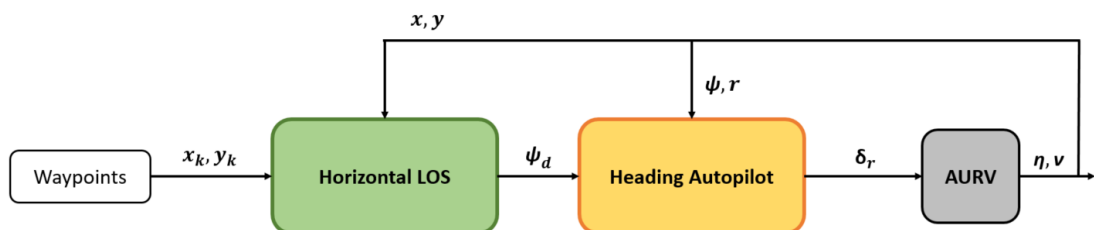


Figure 3.1: Block diagram of the LOS guidance for the horizontal plane

3.1 LOS - Line of Sight

We begin by deriving the kinematic models associated with equation (2.7), using Euler angles [14] [15].

The first model considers only absolute velocities:

$$\dot{x} = u \cos(\psi) \cos(\theta) - v \sin(\psi) + w \cos(\psi) \sin(\theta), \quad (3.1)$$

$$\dot{y} = u \sin(\psi) \cos(\theta) + v \cos(\psi) + w \cos(\psi) \sin(\theta), \quad (3.2)$$

$$\dot{z} = -u \sin(\theta) + w \cos(\theta), \quad (3.3)$$

$$\dot{\theta} = q, \quad (3.4)$$

$$\dot{\psi} = \frac{r}{\cos(\theta)}, \quad \cos(\theta) \neq 0. \quad (3.5)$$

The second model incorporates relative velocities:

$$\dot{x} = u_r \cos(\psi) \cos(\theta) - v_r \sin(\psi) + w_r \cos(\psi) \sin(\theta) + u_c^n, \quad (3.6)$$

$$\dot{y} = u_r \sin(\psi) \cos(\theta) + v_r \cos(\psi) + w_r \cos(\psi) \sin(\theta) + v_c^n, \quad (3.7)$$

$$\dot{z} = -u_r \sin(\theta) + w_r \cos(\theta) + w_c^n, \quad (3.8)$$

$$\dot{\theta} = q, \quad (3.9)$$

$$\dot{\psi} = \frac{r}{\cos(\theta)}, \quad \cos(\theta) \neq 0. \quad (3.10)$$

where:

$$u_r = u - u_c^b, \quad (3.11)$$

$$v_r = v - v_c^b, \quad (3.12)$$

$$w_r = w - w_c^b, \quad (3.13)$$

with (u_c^b, v_c^b, w_c^b) representing the ocean current velocities in the Body-fixed frame, and (u_c^n, v_c^n, w_c^n) denoting the ocean current velocities in the NED frame.

We consider a 2D continuous path, composed of N waypoints in the xy -plane. Assuming that the motion is constrained to a horizontal plane, where $\theta = 0$, the kinematic equations reduce to:

$$\dot{x} = u \cos(\psi) - v \sin(\psi), \quad (3.14)$$

$$\dot{y} = u \sin(\psi) + v \cos(\psi), \quad (3.15)$$

$$\dot{\psi} = r. \quad (3.16)$$

For a straight-line path between two consecutive waypoints WP_k and WP_{k+1} , the vehicle is required to converge to this trajectory. In the horizontal plane, the

along-track and cross-track errors of the vehicle position (x, y) are defined as:

$$\begin{bmatrix} x_e \\ y_e \end{bmatrix} = R^T(\gamma_p) \begin{bmatrix} x - x_k \\ y - y_k \end{bmatrix}, \quad (3.17)$$

where:

- (x_k, y_k) represents the position of the k -th waypoint in the NED frame,
- $R(\gamma_p)$ is the rotation matrix from the inertial frame to the path-fixed reference frame, given by:

$$R(\gamma_p) = \begin{bmatrix} \cos(\gamma_p) & -\sin(\gamma_p) \\ \sin(\gamma_p) & \cos(\gamma_p) \end{bmatrix}, \quad (3.18)$$

where γ_p denotes the horizontal path-tangential angle, defined as:

$$\gamma_p = \text{atan2}(y_{k+1} - y_k, x_{k+1} - x_k). \quad (3.19)$$

Consequently, we obtain:

$$x_e = (x - x_k) \cos(\gamma_p) + (y - y_k) \sin(\gamma_p), \quad (3.20)$$

$$y_e = -(x - x_k) \sin(\gamma_p) + (y - y_k) \cos(\gamma_p). \quad (3.21)$$

In marine guidance applications, the LOS vector originates from a reference point (the vehicle) and extends to a point (x_{los}, y_{los}) on the path-tangential line, located at a lookahead distance $\Delta_h > 0$ from the direct projection of the vehicle position $p(x, y)$ onto the path. The geometry of the guidance system is illustrated in [Figure 3.2], together with the key variables involved.

The choice of Δ_h significantly influences the vehicle's maneuverability: a smaller Δ_h results in sharper steering, while a larger Δ_h leads to smoother trajectories. While adaptive strategies for dynamically adjusting Δ_h have been explored in previous studies, this work assumes a constant $\Delta_h = 0.05m$ to simplify analysis and enable a more consistent performance comparison across different guidance laws.

The lookahead-based guidance law is expressed as:

$$\psi_d = \gamma_d + \arctan\left(\frac{-y_e}{\Delta_h}\right). \quad (3.22)$$

In the presence of external disturbances such as ocean currents, the heading angle ψ_d and the course angle χ_d are related as follows:

$$\chi_d = \psi_d + \beta, \quad (3.23)$$

$$\beta = \text{atan2}(u, v). \quad (3.24)$$

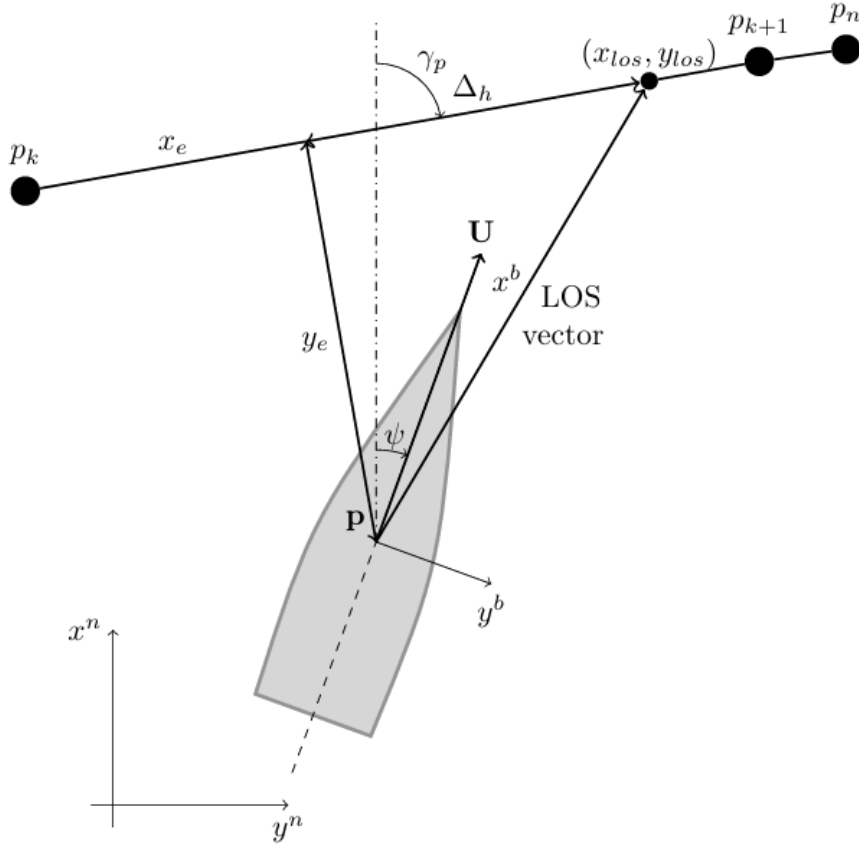


Figure 3.2: LOS geometry for straight lines in the xy plane

Thus, the desired heading angle is given by:

$$\psi_d = \gamma_d + \arctan\left(\frac{-y_e}{\Delta_h}\right) - \text{atan2}(u, v). \quad (3.25)$$

Finally, the heading error is computed as:

$$\delta_r = \psi_d - \psi. \quad (3.26)$$

This error is then provided as input to the PID controller, which will be detailed in the following chapter.

3.2 PID controller

The control strategy adopted for our system is based on a PID (*Proportional-Integral-Derivative*) controller, whose main objective is to minimize the error $e(t)$

between a desired value and the actual value of the controlled system. The PID is widely used in engineering due to its ability to ensure stability and an adequate dynamic response in a wide range of applications.

A PID controller consists of three main components:

- **Proportional Control (P):** the proportional action is directly proportional to the current error. If the error is large, the control action will be strong, whereas if it is small, the action will be more contained. This helps to react quickly to errors, but alone it may not completely eliminate steady-state error. The coefficient K_p regulates this action:

$$u(t) = K_p e(t)$$

- **Integral Control (I):** the integral action considers the accumulation of error over time, reducing the steady-state error. However, an excessive value of K_i may lead to instability and undesirable oscillations. The coefficient K_i regulates this action:

$$u(t) = K_i \int_0^t x_e(\tau) d\tau$$

- **Derivative Control (D):** the derivative action considers the rate of change of the error, improving response to sudden changes and reducing the risk of oscillations. This component helps predict the system's future behaviour, enhancing overall stability. The coefficient K_d regulates this action:

$$u(t) = K_d \frac{de(t)}{dt}$$

The overall PID control action is obtained by summing the contributions of the three previous components:

$$u(t) = K_p e(t) + K_i \int_0^t e(\tau) d\tau + K_d \frac{de(t)}{dt} \quad (3.27)$$

Formula (3.27) describes the control signal $u(t)$, which will be sent to the system actuators in order to correct the trajectory or position. In the case of a robotic system or an autonomous vehicle, the control signal is converted into mechanical actions, such as adjusting motor speed or changing direction, ensuring that the system follows the desired trajectory as precisely as possible.

In order to control a system with multiple DOF, a separate PID controller is required for each independent movement. In the case of horizontal LOS control, two primary PIDs are required:

- PID for position control along the X-axis
- PID for Yaw-angle control

A PID for position control along the Y-axis is not possible, due to the configuration of the motors of RUVIFIST.

The parameters K_p , K_i , and K_d are generally determined using tuning techniques, which may include empirical methods such as *trial and error*, or more sophisticated algorithms like model-based optimization.

For horizontal LOS control, the chosen PID parameters are summarized in table 3.1.

PID Controller	K_p	K_i	K_d
X Position Control	35.00	0.10	20.00
Yaw Control	80.00	0.15	35.00

Table 3.1: PID gains for position and yaw control

These values were selected to ensure a stable and efficient system response, minimizing error and limiting undesirable oscillations. In addition, proper PID parameter tuning optimizes system performance, improving both reference tracking accuracy and robustness against external disturbances.

Chapter 4

Simulations and results

In this chapter, we will analyze the performance of RUVIFIST in executing different trajectories, using the simulation model (Fossen model) presented in chapter 2. The study will be structured around four trajectories of increasing complexity, allowing us to evaluate the effectiveness of the PID controller and LOS driving strategy described in sections 3.2 and 3.1.

Our analysis will focus on overall performance, considering factors such as trajectory precision, motion fluidity and engine response; we will also examine the effects of waypoint density and motor saturation when relevant, along with the forces acting on the system, including drag and inertia.

The objective is to evaluate the vehicle's dynamic response to the controller configuration and its ability to follow predefined paths and potential improvements in navigation accuracy and control.

4.1 First trajectory: straight line

The first trajectory analyzed is a diagonal straight line. The results of this simulation are shown in [Figure 4.1], [Figure 4.2] and [Figure 4.5].

Given that the TCM is designed in such a way that the vehicle cannot move purely along the Y-axis, the AUV first rotates to align with the desired heading and then proceeds along that direction.

Regarding propulsion, the evolution of forces and moments follows this principle: in the force graph, the Yaw moment initially increases rapidly as the vehicle begins to rotate, then gradually decreases to zero once the desired orientation is reached. Simultaneously, the force in the X direction increases until it stabilizes at a constant value, allowing the AUV to move forward at a steady velocity.

For motor actuation, we observe that initially, the motors on the left side (Motor 1 and Motor 3) generate a stronger thrust compared to those on the right side

(Motor 2 and Motor 4) to enable the vehicle to change its orientation. Once the desired heading is achieved, all four motors adjust to a constant thrust level to maintain a uniform forward velocity.

4.2 Second trajectory: L-shape

The second trajectory analyzed is an L-shaped path. The results of this simulation are shown in [Figure 4.3], [Figure 4.4] and [Figure 4.6].

As observed in the straight-line trajectory, the TCM does not allow the vehicle to move purely along the Y-axis. Consequently, the AUV first moves straight along the X-axis. Upon reaching the waypoint at the corner, it rotates 90° to the right and then proceeds along the new heading. This behavior is consistent with the propulsion data shown in the graph: initially, the motors operate at a constant thrust to cover the forward segment along the X-axis. Then, similar to the previous trajectory, the motors on the left side (Motor 1 and Motor 3) are actuated in the opposite direction to those on the right side (Motor 2 and Motor 4) to enable the 90° rotation. Once the turn is complete, the motors return to the previous configuration to continue along the final segment of the trajectory. The principle of first rotating and then moving is beneficial because drag is minimized when the vehicle moves frontally, leading to more efficient energy consumption.

One notable aspect of this trajectory is the slight uncertainty at the corner: during the rotation around the Z-axis, the vehicle momentarily loses precision in maintaining the target waypoint. This is also evident in the force and moment graphs, where the X-direction force briefly drops to a negative value near the point at which the AUV changes orientation. However, this deviation is minimal (approximately 0.25 m on a 2 m vehicle) and is therefore negligible for our analysis. Nonetheless, a more refined PID controller could further reduce this error.

4.3 Third trajectory: smooth curve

The third trajectory analyzed consists of a straight segment followed by a leftward curve. The results of this simulation are shown in [Figure 4.7], [Figure 4.8] and [Figure 4.11].

While the general principles from the previous trajectories still apply, it is possible to see an important difference: the AUV's executed path does not perfectly align with the input trajectory. This discrepancy occurs because, during the straight segment, the vehicle gains significant kinetic energy due to its forward velocity. The vehicle's high inertia, caused by its long and slender shape, leads to resistance when attempting to change direction as it enters the curve. This resistance results

in drift, or *derapage*, causing the AUV to deviate from the intended trajectory during the turn.

This drift is evident in the propulsion data, where the controller generates corrective forces to realign the vehicle. However, due to the high inertia and momentum carried over from the straight segment, the corrections are not instantaneous, leading to oscillations or overshoot. In order to mitigate this issue, more advanced control strategies, such as feedforward control or model predictive control (MPC), could better anticipate the vehicle's dynamic behavior and smooth out the corrective efforts.

4.4 Fourth trajectory: S-path

The fourth trajectory analyzed is an S-path, generated using a cubic function, which presents a more complex path compared to the previous ones. This maneuver is not typically performed by our AUV; however, we simulate it to represent an obstacle avoidance scenario and evaluate the trajectory tracking accordingly. The results of this simulation are shown in [Figure 4.9] and [Figure 4.10].

Despite the PID controller not being highly precise, the achieved trajectory remains closely aligned with the reference path. The vehicle effectively follows the intended course, demonstrating the robustness of the control approach in managing complex maneuvers. With further refinement, particularly through parameter optimization, trajectory tracking could be further enhanced, leading to even greater accuracy and responsiveness in real-world applications.

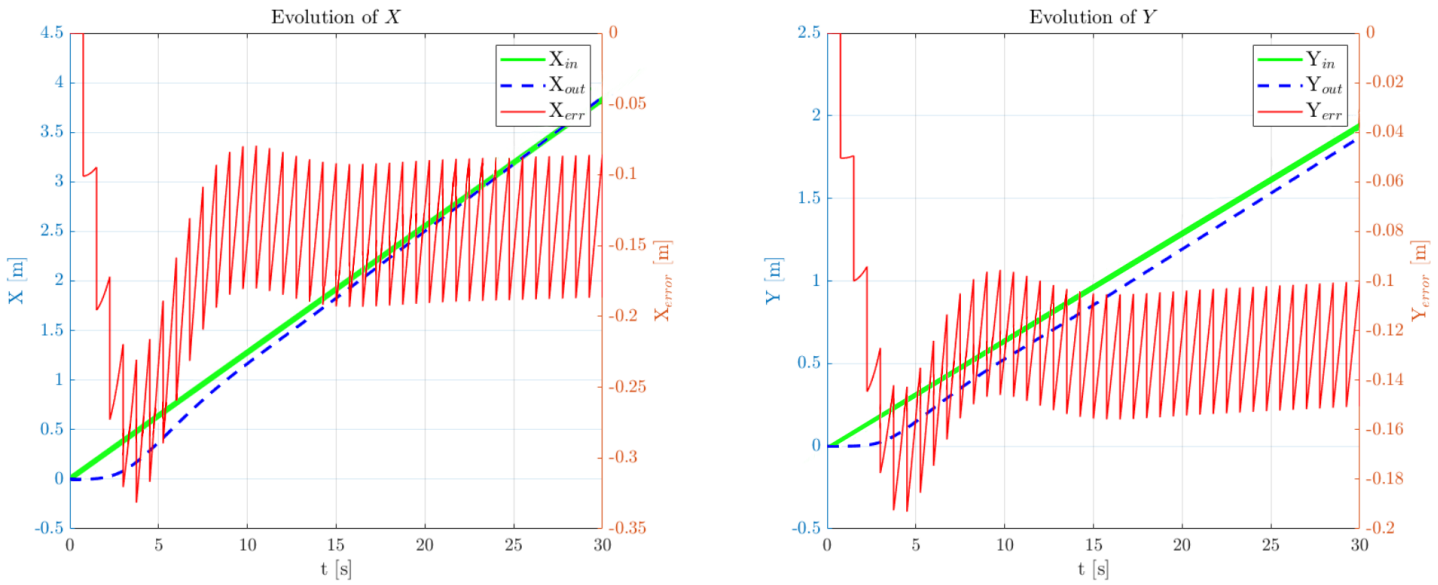


Figure 4.1: First trajectory: evolution of X and Y

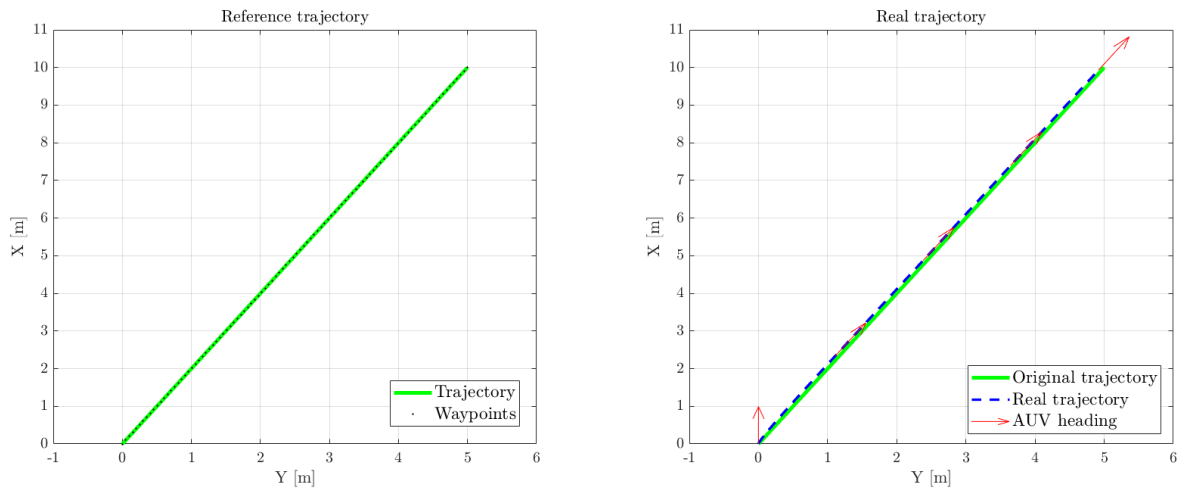


Figure 4.2: First trajectory: trajectories comparison

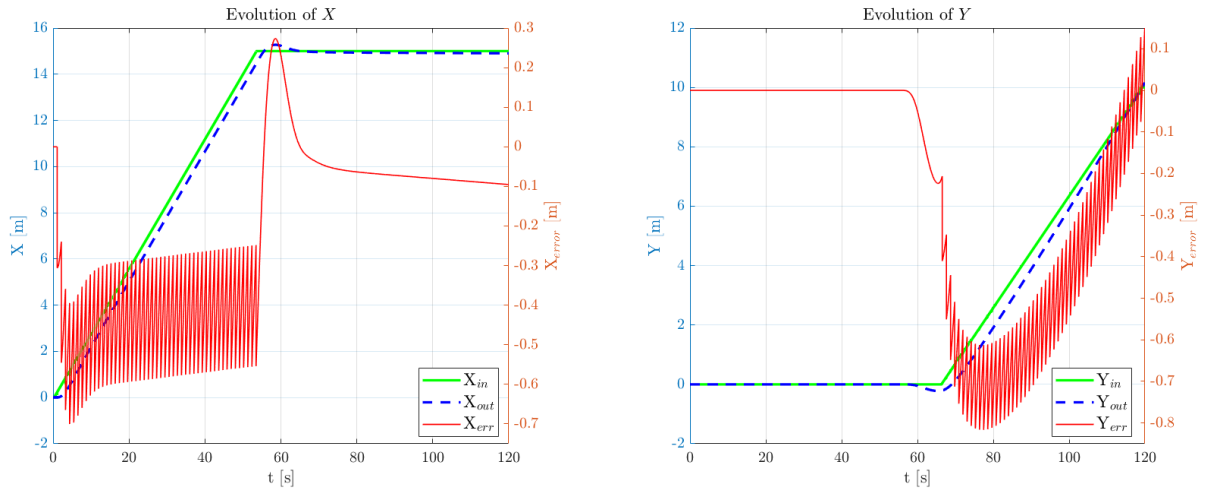


Figure 4.3: Second trajectory: evolution of X and Y

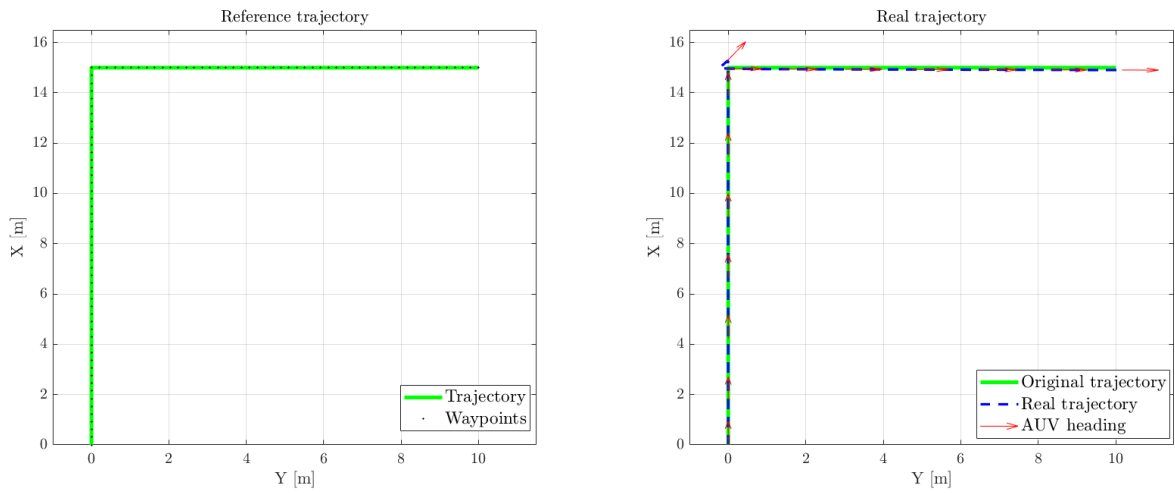


Figure 4.4: Second trajectory: trajectories comparison

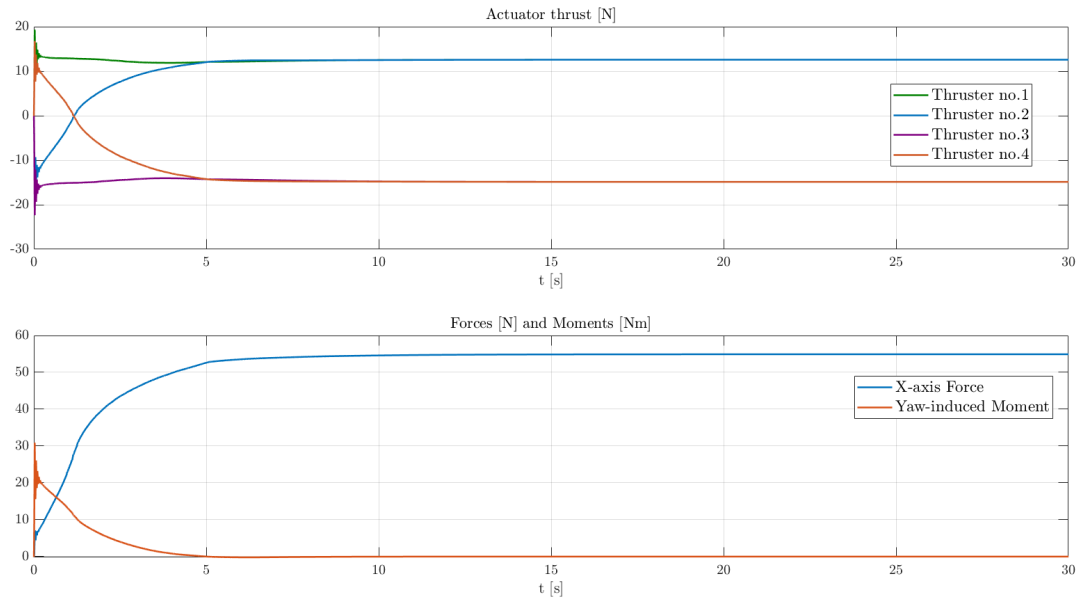


Figure 4.5: First trajectory: propulsion

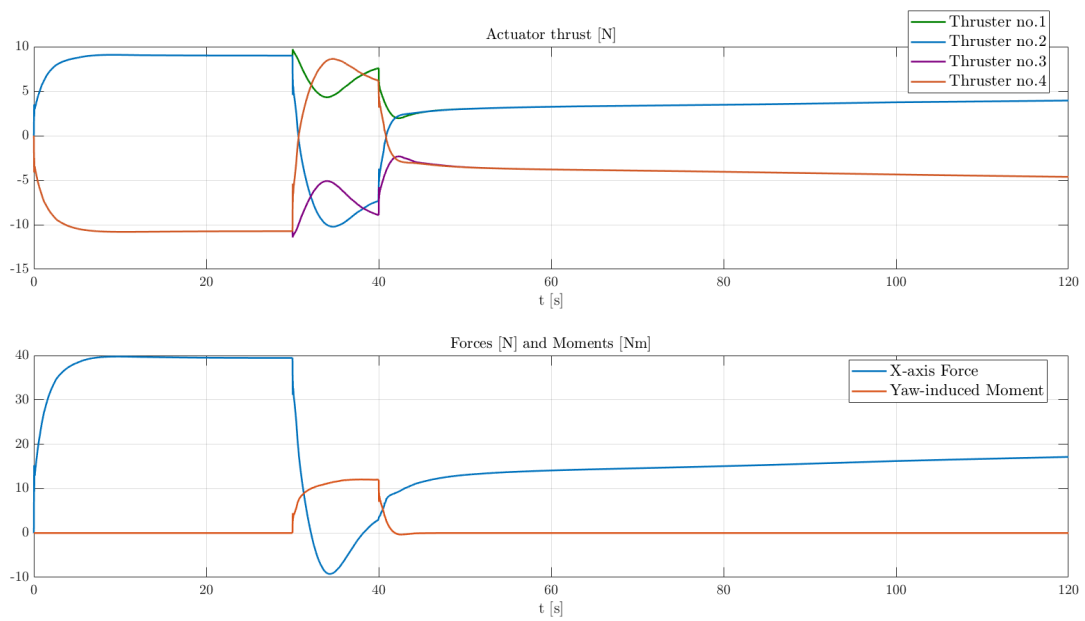


Figure 4.6: Second trajectory: propulsion

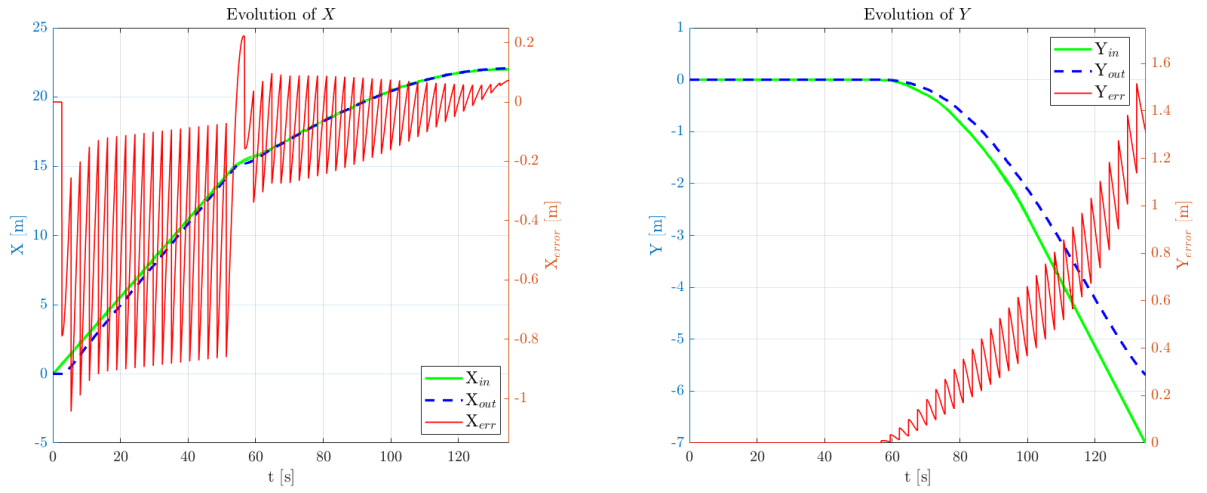


Figure 4.7: Third trajectory: evolution of X and Y

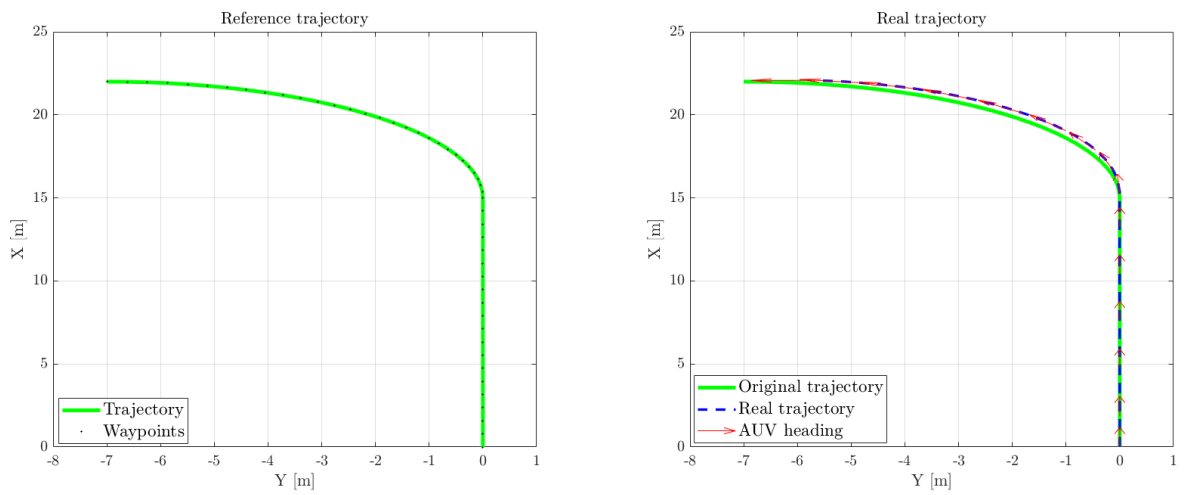


Figure 4.8: Third trajectory: trajectories comparison

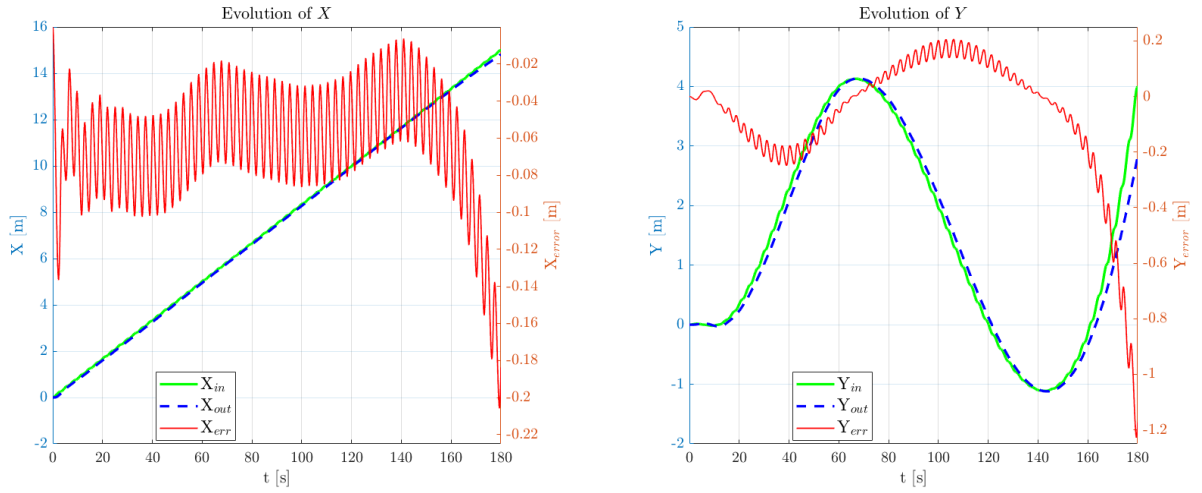


Figure 4.9: Fourth trajectory: evolution of X and Y

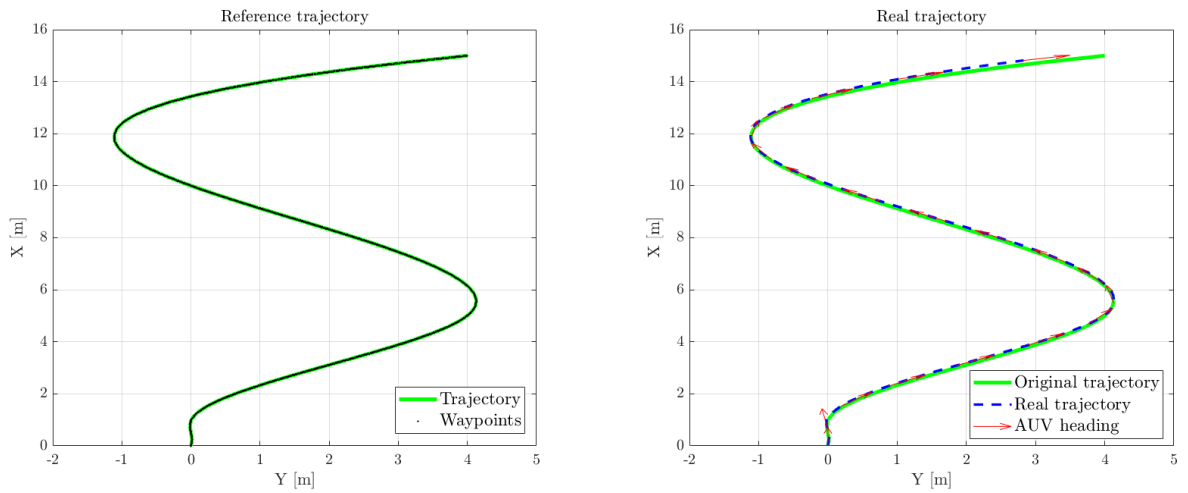


Figure 4.10: Fourth trajectory: trajectories comparison

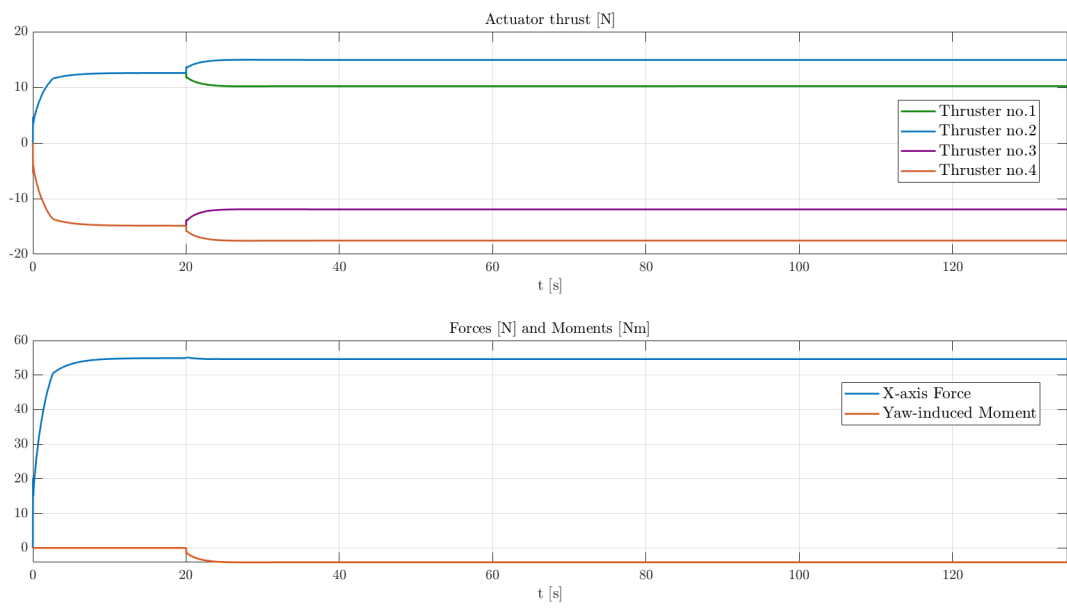


Figure 4.11: Third trajectory: propulsion

Part II

Chapter 5

Problem definition

As previously outlined, RUVIFIST is an AURV designed to efficiently reconfigure its shape according to the task at hand, spanning from a survey slender configuration [Figure 5.1] to a hovering sturdy layout [Figure 5.2].

The transformation is made possible due to the presence of six joints: two active ones, which use a worm drive system paired with a M200 motor, and four passive ones, which allow for flexibility and movement without actuation.

In order to perform this transformation correctly, the system of joints must ensure its proper functioning. More specifically, it is essential that the passive joints maintain symmetry in opening and closing of the layout, even in the presence of external disturbances. At present, the rotation of the passive joints is limited by mechanical end-stop systems, both in opening and closing; however, the joint is free in the intermediate position, compromising the symmetry of the AURV.

Therefore, a positioning system is required to control the position of the joints.

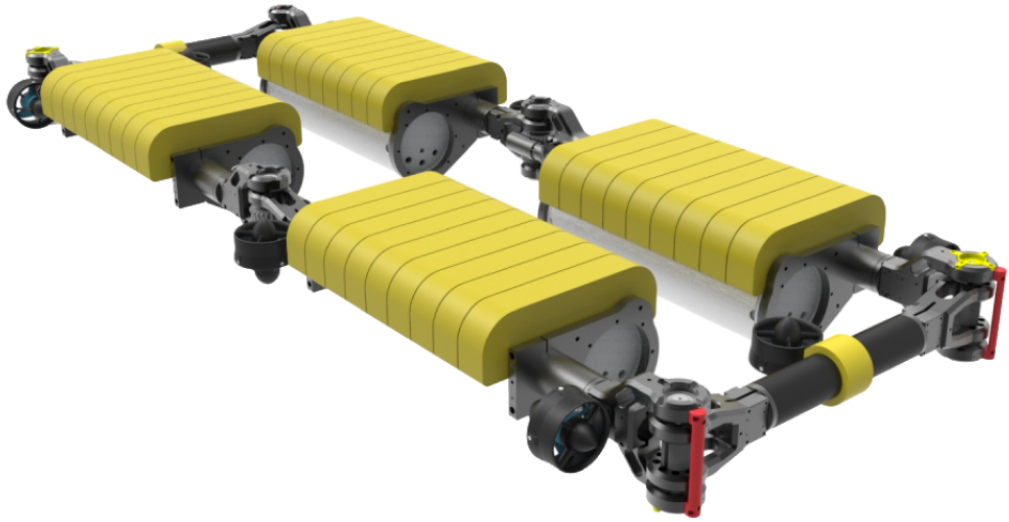


Figure 5.1: Survey configuration

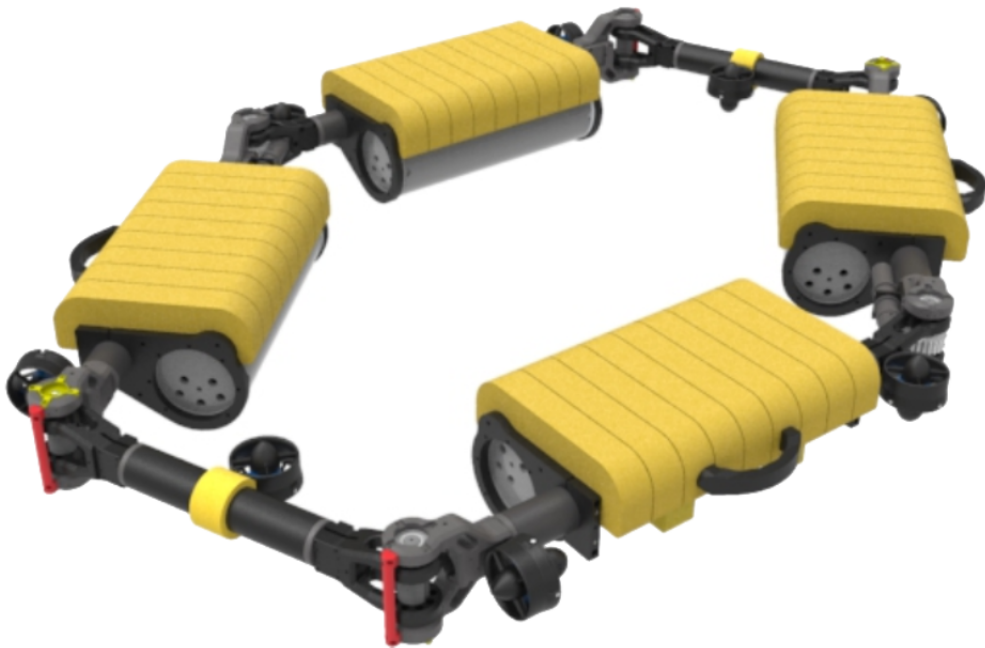


Figure 5.2: Hovering configuration

Chapter 6

Pulley design

We will consider a parallel-axis belt drive, in which the belt wraps continuously around curved sections of the pulleys, ensuring contact over a certain angle. However, in this system, the pulleys do not actively drive the belt but only serve to maintain a defined relative position with respect to each other. The tension exerted on one of the two branches of the belt, as a result of the application of a driving force, helps maintain the correct alignment between the pulleys. To ensure proper system operation, the belt must be pre-tensioned, ensuring adequate grip between the belt and the pulleys.

The designed pulley adopts a cross configuration [Figure 6.1], chosen to ensure that two joints open and close synchronously, even in the presence of external disturbances. In this configuration, the two branches of the belt experience alternating variations in tensile load relative to the initial pre-tension: while one branch undergoes an increase in tension, the other experiences a reduction. Unlike a system with a parallel belt arrangement, which maintains the same direction of rotation for the pulleys, the cross configuration reverses the direction of rotation between the two pulleys, generating a mirrored movement essential for the correct functioning of our system.

6.1 Rope Material

After choosing the cross-configuration type of pulley it was decided to optimise the transmission mechanism by using two ropes wrapped in a spiral hollow, in order to further improve the efficiency of the system. This solution allows for better distribution of forces and ensures greater synchronization of movement, thus increasing the reliability and accuracy of the system as a whole.

The chosen ropes are made of *Dyneema SK78* [16] for their strength and lightness, which helps to reduce the overall weight without compromising the load capacity

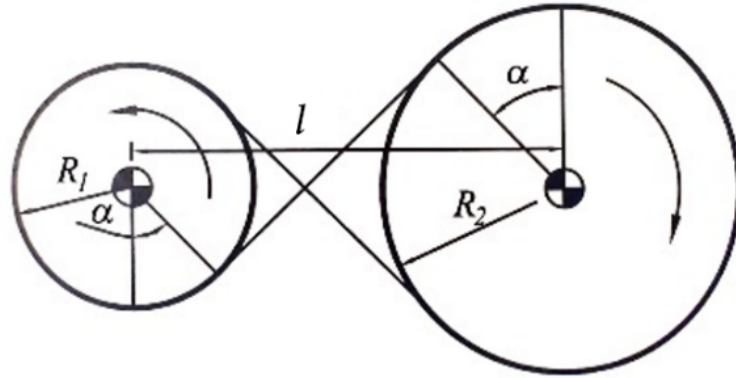


Figure 6.1: Cross configuration

of the system. The characteristics of the rope are shown in table 6.1:

Construction	Single braid
Diameter \varnothing [mm]	4
SWL [kg]	600
NBL [kg]	1500
Weigth per meter [g]	8.8
Elastic modulus [GPa]	33.45

Table 6.1: *Dyneema SK78* characteristics

6.2 Pulley groove

We choose a trapezoidal groove for the following reasons:

- Improved grip and torque transmission: the trapezoidal shape allows the belt to have a larger contact surface with the pulley than a flat hollow. This ensures more efficient torque transfer and reduces the risk of slipping
- Better distribution of forces: the trapezoidal section of the belt evenly distributes forces along the inclined sides, reducing stress concentration and increasing the life of both the belt and pulley
- Automatic alignment and centering: the trapezoidal shape makes the belt stay centered in the groove during operation, reducing the risk of misalignment

In addition, a spiral shaft [Figure 6.4] was chosen instead of a straight one for several advantages: firstly, it allows a more even distribution of the tension along the whole length of the rope, thus reducing the risk of slipping and improving the transmission of the movement. In addition, the spiral hollow allows a greater angle of winding of the rope around the pulley, increasing grip and thus the ability to transmit torque without excessive wear.

The parameters of the groove will now be determined.

Given the diameter of the rope $d = 4$ mm, the following formulae are applied, with reference to [Figure 6.2]:

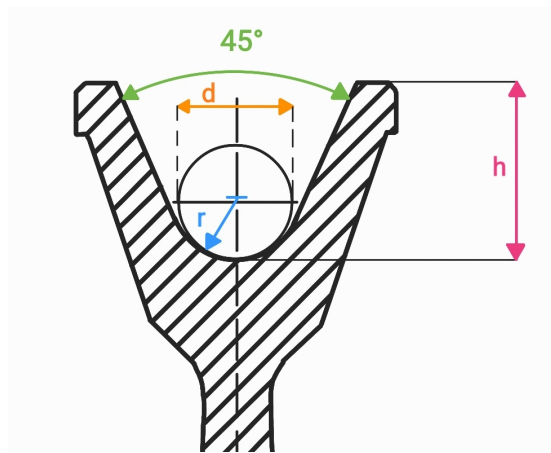


Figure 6.2: Groove parameters scheme

- Depth of the groove

$$h = 1.5d \text{ to } 2d \quad (6.1)$$

- Radius of the groove

$$r \approx 1.05 \cdot \frac{d}{2} \quad (6.2)$$

We choose a depth of the groove $h = 1.75d = 7$ mm according to (6.1), thus obtaining a radius of $r = 2.1$ mm.

This configuration ensures optimal force distribution and enhances the longevity of the system.

6.3 Rope parameters

In order to proceed with the pulley design, it is useful to determine the minimum usable length of the rope L , as a function of the center-to-center distance l and the pulleys' radii R_1 and R_2 [17].

From the data provided by the *SolidWorks* model, we know that $l = 570$ mm [Figure 6.3].

The pulley to be designed must be rigidly connected to the passive joint; we consider an external diameter of $D = 100$ mm.

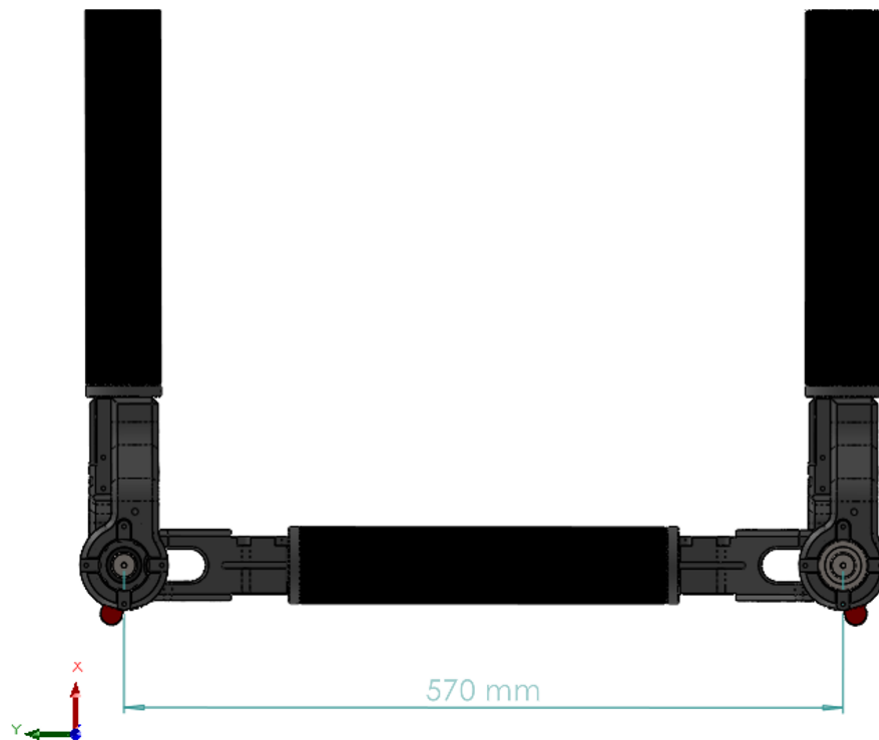


Figure 6.3: CAD model for the beta test

With reference to the geometry of [Figure 6.1], the angles of the belt's embrace are given by:

$$\theta_1 = \theta_2 = \pi + 2\alpha \quad (6.3)$$

where, recalling that $l = 570$ mm is the center-to-center distance between the two pulleys:

$$\alpha \approx \sin \alpha = \frac{R_2 + R_1}{l} \quad (6.4)$$

We determine the radius of the pulley by reference to [Figure 6.2]: given the external diameter $D = 100$ mm, the depth of the groove $h = 7$ mm and the rope diameter $d = 4$ mm, it is possible to compute the radius R_R around which the rope is wrapped on the pulley as follows:

$$R_R = \frac{D}{2} - h + \frac{d}{2} = 45 \text{ mm} \quad (6.5)$$

In our case study, the designed pulleys will have the same dimensions, thus:

$$R_2 = R_1 = R_R = 45 \text{ mm} \quad (6.6)$$

and the equation (6.4) becomes:

$$\alpha \approx \sin \alpha = \frac{R + R}{l} = \frac{2R}{l} = 0.158 \text{ rad} = 9.05^\circ \quad (6.7)$$

By summing the lengths of the two circular and straight sections of the belt, we obtain:

$$L = \theta_1 R_1 + \theta_2 R_2 + 2l \cos \alpha \quad (6.8)$$

Taking into account that:

$$\cos \alpha \approx 1 - \frac{\alpha^2}{2} = 1 - \frac{(R_2 + R_1)^2}{2l^2} \quad (6.9)$$

$$\alpha \approx \sin \alpha = \frac{R_2 + R_1}{l} \quad (6.10)$$

Equation (6.8) simplifies as follows:

$$L = (\pi + 2\alpha)R_R + (\pi + 2\alpha)R_R + 2l \left(1 - \frac{(R_R + R_R)^2}{2l^2} \right) = 2\pi R_R + 2l + \frac{4R_R^2}{l} \quad (6.11)$$

The minimum total length of the rope to be used is:

$$L = 1437 \text{ mm} \quad (6.12)$$

The actual length of the rope will be significantly longer because, as will be shown in the following chapters, the configuration of the tensioning system requires that the rope can wrap at least twice around the pulley.

6.4 Pulley body

A beta version of the pulley was designed for testing purposes [Figure 6.4]. This pulley consists of three main sections, each with a specific function to ensure stability, efficiency and safety in the transmission system.

- Upper cover: it has a cross structure designed for the pulley hub to the bottom of the passive joint, which is firmly fixed by four threaded bars.
- Central body: rigidly attached to the top, it is characterized by the presence of six turns, designed to allow double winding of each of the two ropes, as shown in the scheme of [Figure 6.5]. The ropes are firmly locked inside the pulley, Ensuring a secure anchorage and preventing accidental slippage.
- Lower cover: equipped with a lid, which if open allows the inspection of the internal layout. The ropes are secured by a safety node [Figure 6.6], designed to prevent the risk of derailment and ensure reliable operation of the system.



Figure 6.4: Beta pulley

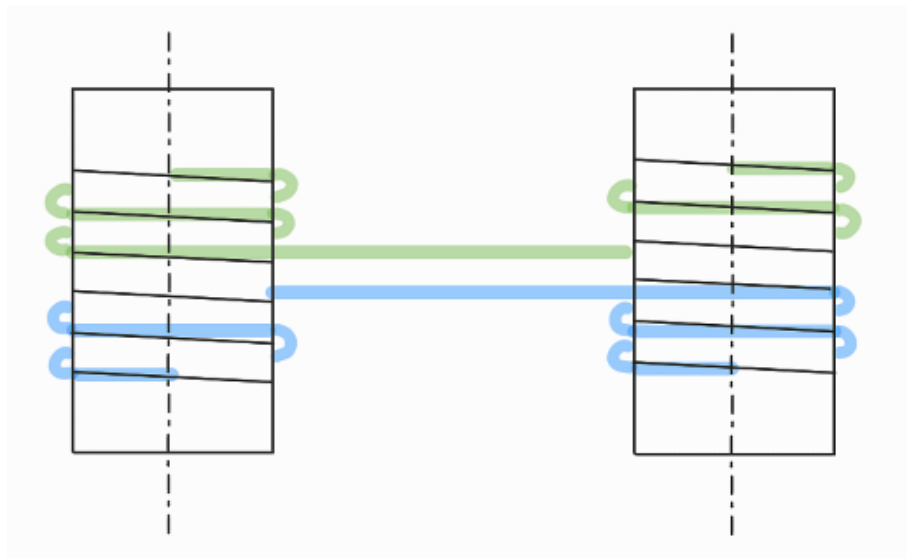


Figure 6.5: Rope configuration scheme



Figure 6.6: Safety node

Chapter 7

Beta pulley experimental testing

7.1 Dry testing

In order to test the system's efficiency, dry tests were conducted. In these tests, the right joint [Figure 7.1] was kept still while an external disturbance was simulated, with the help of a load cell [Figure 7.2], on the other joint by applying a force F_d at a distance $b_d = 115$ mm from the rotation axis, as shown in [Figure 7.3]. The force was applied at different intervals and the joint opening was measured using an encoder integrated into the joint. The rope tension was measured before and after each test using a load cell, with the expectation of detecting any failure of the rope.



Figure 7.1: Beta pulleys testing



Figure 7.2: Load cell simulating the external disturbance F_d

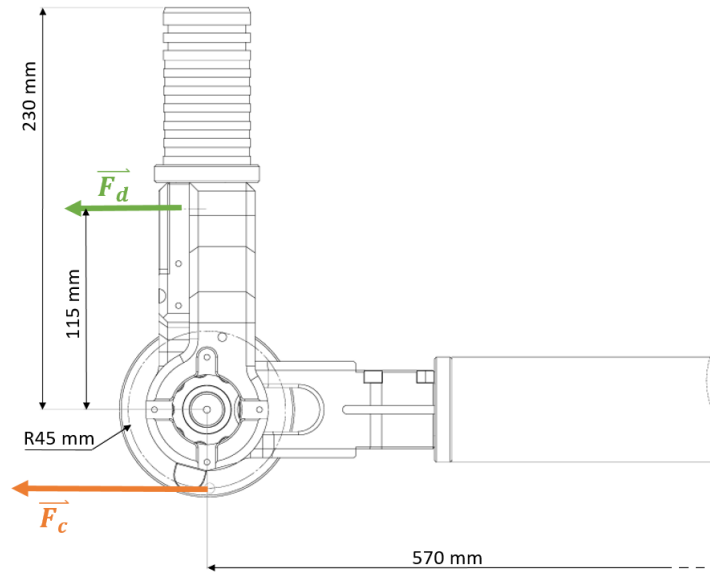


Figure 7.3: Joint configuration

Three tests were conducted: the system was preloaded before each measurement, with a different preload applied for each test.

In order to determine the force applied on the rope, we consider $b_d = 115$ mm as the lever arm relative to the rotation axis of the joint and $b_c = 45$ mm as the lever arm where the rope experiences the force F_c [Figure 7.3]. The force applied on the rope was calculated using the equilibrium of moments as follows:

$$F_c = F_d \cdot \frac{b_d}{b_c} \quad (7.1)$$

The results of these measurements are reported in tables 7.1, 7.2, and 7.3.

Force to open the joint [kg]	Force applied on the rope [kg]	Joint opening [°]
0.00	0.00	0.272
4.50	11.50	0.272
9.50	24.28	2.469
14.00	35.78	4.149
18.50	47.28	6.864
23.00	58.78	9.413
28.00	71.56	10.083

Table 7.1: First test

Force to open the joint [kg]	Force applied on the rope [kg]	Joint opening [°]
0.00	0.00	0.272
4.20	10.73	0.272
8.50	21.72	1.041
14.00	35.78	3.085
18.00	46.00	4.491
23.00	58.78	5.809
29.00	74.11	10.028

Table 7.2: Second test

Force to open the joint [kg]	Force applied on the rope [kg]	Joint opening [°]
0.00	0.00	0.272
3.90	9.97	0.272
8.90	22.74	0.799
13.30	33.99	2.909
18.00	46.00	3.964
23.00	58.78	5.809
27.50	70.28	8.023

Table 7.3: Third test

Preload [kg]	Before the test	After the test
Test 1	6.00	3.20
Test 2	11.80	5.20
Test 3	14.20	10.60

Table 7.4: Preload values of the rope

Based on the results obtained, the following considerations can be made:

- In the design of the pulley, a tie-down knot on the ropes was provided for safety reasons [Figure 7.7], with the aim of avoiding the risk of derailment. However, during the experimental tests, it was observed that this node does not come into tension during operation, due to friction between pulley and rope.
- The failure behaviour of the joint, in degrees, is illustrated in [Figure 7.4], showing the progressive variation of the opening angle as a function of the torque applied during the experimental tests.
As shown in table 7.4, after each test it was necessary to increase the preload of the rope. This is due to a loss of rope tension caused by micro-sliding of the rope on the pulley grooves, which occurs at each load iteration.

The experimental results will now be compared with a FEM (Finite Elements Method) simulation on *SolidWorks*, using data from both the test and the material datasheet. This allow to assess the consistency of the model and validate its behaviour.

7.2 Validation on FEM simulation studies

In absence of specific tensile tests to characterize the actual rope, the system will be validated using an elastic modulus value found from the data obtained from the experimental test, being compared with an ideal system considering the data of a *Dyneema SK78* rope, with a module of Young $E = 33.45$ GPa, as shown in table 6.1.

Since it was not possible to measure the micro-sliding between the rope and the pulley cavity, these were included in a comprehensive evaluation of the behaviour of the rope, representing the latter as a rigid rod. This approach allowed the development of a CAD model with characteristics equivalent to the real configuration, which was used for FEM analysis. This choice represents a significant simplification of the model, made necessary by the limitations of the available software in the accurate modelling of the rope.

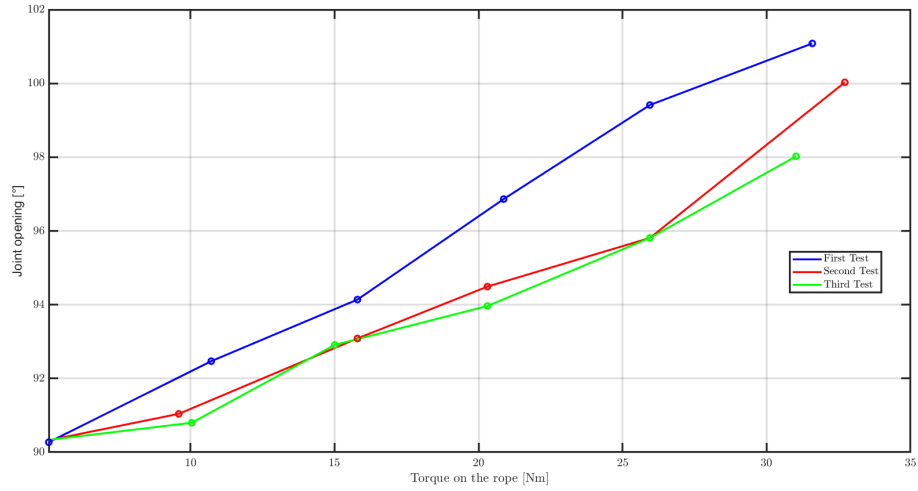


Figure 7.4: Failure behaviour of the joint during beta testing

In real-world applications, the use of a rope instead of a rigid rod is justified by its ability to provide damping, reducing impacts and shocks on joints and preventing potential damage. In addition, the rope is lighter and more cost-effective compared to a rigid shaft.

7.2.1 Simulation with experimental parameters

In order to perform the FEM simulation, it is necessary to determine a value of the elastic module to be applied to the rigid rod. This value is obtained from the experimental data of the third test.

The elastic module E is defined as:

$$E = \frac{\sigma}{\varepsilon} \quad (7.2)$$

where:

- σ is the stress computed as the ratio between the applied force and the section area of the rope.
- ε is the strain defined as the ratio between the elongation ΔL and the initial length of the rope L_0 .

Computation of stress σ

Stress σ is defined as:

$$\sigma = \frac{F}{A} \quad (7.3)$$

Considering the force applied to the rope, as reported in table 7.3:

$$F = 70.28 \text{ kg} = 689.45 \text{ N} \quad (7.4)$$

The cross-sectional area of the rope, given a diameter $d = 4 \text{ mm}$, is:

$$A = \frac{\pi}{4} d^2 = 12.57 \text{ mm}^2 \quad (7.5)$$

From these values, the value of the stress applied is computed:

$$\sigma = \frac{F}{A} = \frac{689.45}{12.57} = 54.86 \text{ MPa} \quad (7.6)$$

Computation of strain ε

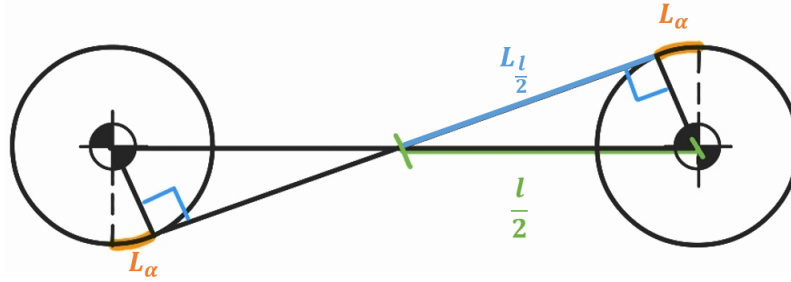


Figure 7.5: Pulley scheme no.1

Strain ε is defined as:

$$\varepsilon = \frac{\Delta L}{L_0} \quad (7.7)$$

The initial length of the rope consists of the segment that connects the two pulleys and the wrap angles α , as shown in [Figure 7.5].

Considering the rope segment wrapped around the pulley:

$$L_\alpha = \frac{C}{360} \cdot \alpha = 7.1 \text{ mm} \quad (7.8)$$

where, with reference to chapter 6.3:

- $\alpha = 9.05^\circ$
- C is the circumference of the pulley, defined as: $C = 2\pi R_R$ with $R_R = 45 \text{ mm}$

The portion of the rope connecting the two pulleys, as shown in [Figure 7.6], is given by:

$$L_{l/2} = 2 \cdot \sqrt{R_R^2 + \frac{l^2}{4}} = 577.06 \text{ mm} \quad (7.9)$$

Combining equations (7.4) and (7.5), the initial belt length before load application is:

$$L_0 = L_{l/2} + 2L_\alpha = 591.27 \text{ mm} \quad (7.10)$$

Considering additional rope sections wrapped around the pulleys and the internal segment, as shown in [Figure 7.6], the final approximated initial rope length is obtained by multiplying by 2.5:

$$L_{0 \text{ approx}} = 1478.17 \text{ mm} \quad (7.11)$$

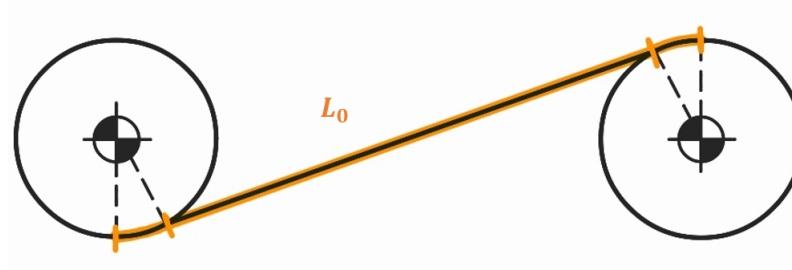


Figure 7.6: Pulley scheme no.2

We now compute the elongation ΔL . From table 7.3, the joint undergoes a rotation of:

$$\beta = 98.023^\circ - 90.272^\circ = 7.75^\circ \quad (7.12)$$

The elongation ΔL_{ex} of the test is computed as the arc length corresponding to this angular variation:

$$\Delta L_{ex} = \frac{C}{360} \cdot \beta = 6.1 \text{ mm} \quad (7.13)$$

Thus, from equation (7.7) the experimental strain is:

$$\varepsilon_{ex} = \frac{\Delta L_{ex}}{L_0} = \frac{6.1}{1478.17} = 0.0041 \quad (7.14)$$

And from equation (7.2), the experimental elastic modulus is:

$$E_{ex} = \frac{\sigma}{\varepsilon_{ex}} = 13.38 \text{ GPa} \quad (7.15)$$



Figure 7.7: Experimental parameters - displacement along the y direction [mm]

This value will be used in the FEM simulation to verify the consistency of the model with experimental data. The simulation will be performed with a load of 31 Nm, consistent with the maximum force applied during experimental tests.

From the FEM analysis results [Figure 7.7], a displacement along the y - axis of 31.04 mm is observed.

Using trigonometry, the maximum failure angle of the test γ_{ex} is computed as:

$$y = a \cdot \sin(\gamma_{ex}) \quad (7.16)$$

$$\gamma_{ex} = \arcsin\left(\frac{y}{a}\right) = 7.76^\circ \quad (7.17)$$

Where $a = 230$ mm is the fork length, as indicated in [Figure 7.3].

These values demonstrate a high degree of consistency with the experimental measurements (7.75°), confirming the validity of the adopted model and its ability to accurately reproduce the real behaviour of the system.

7.2.2 Simulation with theoretical parameters

We now compare the maximum strain obtained in the previous chapter, $\varepsilon_{ex} = 0.0041$, with the strain obtained from the simulation of the ideal system, ε_{th} , using the

elastic modulus from the datasheet in table 6.1, given as $E_{th} = 33.45$ GPa. The applied stress is equivalent to the value found in equation (7.6):

$$\sigma = \frac{F}{A} = 54.86 \text{ MPa} \quad (7.18)$$

The strain, obtained from equation (7.7), is:

$$\varepsilon_{th} = \frac{\sigma}{E_{th}} = \frac{54.86 \text{ MPa}}{33.45 \text{ GPa}} = 0.0016 \quad (7.19)$$

The elongation of the rope is given by:

$$\Delta L_{th} = L_0 \cdot \varepsilon_{th} = 2.91 \text{ mm} \quad (7.20)$$

Thus, the final length of the rope is:

$$L = L_0 + \Delta L_{th} = 1776.7 \text{ mm} \quad (7.21)$$

It is observed that the elongation of approximately 3 mm is primarily due to the material's compliance.

We now perform an FEM simulation with a load of 31 Nm, consistent with the maximum applied force during experimental tests.

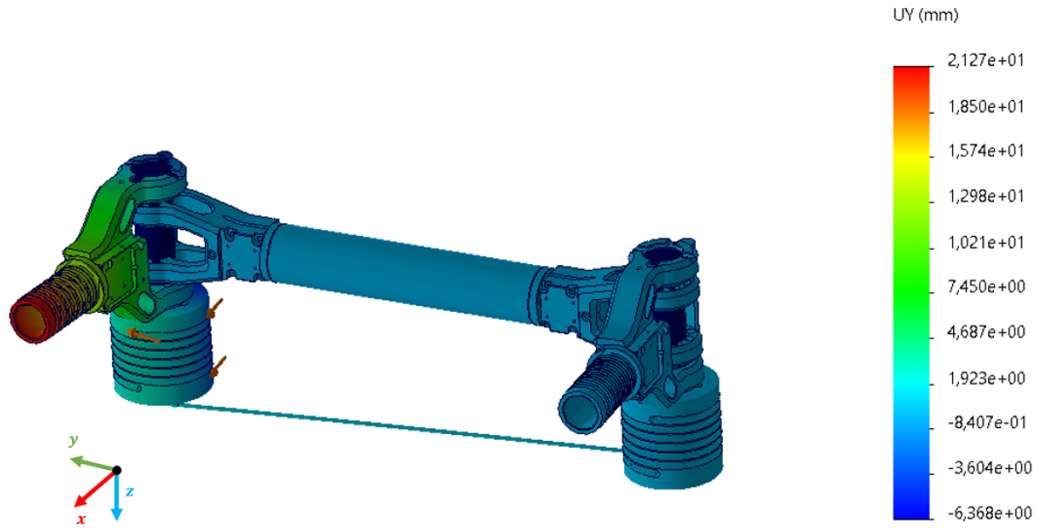


Figure 7.8: Theoretical parameters - displacement along the y direction [mm]

From the analysis of the FEM simulation results [Figure 7.8], a displacement along the y - axis of 21.27 mm is observed.

Using equation (7.17), the maximum failure angle γ_{th} is computed as:

$$\gamma_{th} = \arcsin\left(\frac{y}{a}\right) = 4.99^\circ \quad (7.22)$$

where $a = 230$ mm is the fork length, as indicated in [Figure 7.3].

As expected, the calculated strain is significantly lower than the experimental value since the considered elastic modulus is nearly twice the previous one, confirming the validity of the adopted approach. Additionally, the failure angle observed in the numerical model is indeed lower than the one measured in the real system. Both in the theoretical analysis and experimental conditions, a progressive loss of rope tension is observed, attributed to micro-slippages of the rope within the pulley groove.

It is observed that the elongation measured in the experimental analysis is $\Delta L_{ex} = 6.1$ mm, whereas the theoretical calculation yields $\Delta L_{th} = 2.91$ mm. This discrepancy can be explained by the fact that the theoretical model considers only the material's deformation, while during the experimental test we considered also the sliding between the rope and the pulley grooves.

This phenomenon highlights the necessity for a dynamic tensioning system, capable of compensating for such variations and ensuring a stable and reliable system setup after each cycle of use.

Chapter 8

Tensioning system

In order to ensure an effective tensioning of the rope, a ratchet system has been chosen. This mechanism allows rotation in only one direction, preventing the reverse movement thanks to a locking pawl.

The system consists of:

- Ratchet wheel: equipped with inclined teeth that allow rotation in one direction. The tooth profile is designed to optimize grip and reduce wear.
- Pawl: moving element that fits in the teeth of the wheel, preventing the rotation in the opposite direction and ensuring the maintenance of tension in the system. It can be spring-loaded or gravity-actuated, depending on the application. In our case, a spring-loaded pawl will be designed.
- Release system: a mechanism that allows the pawl to be disengaged to release tension, allowing reverse rotation when necessary. In our case, it is rigidly connected to the pawl.
- Central shaft: it is used as a pivot for the rotation of the ratchet wheel. In some cases, it can be hollow to allow the passage of a rope or a cable to be tensioned.

The two systems considered for this configuration are described below.

8.1 External ratchet system

The first version of the ratchet pulley [Figure 8.1] considered an external ratchet system.

The pulley has a hollow internal structure, designed to accommodate the ratchet mechanism. Inside the pulley, the top cover is rigidly connected with a housing

for rotating the central shaft [Figure 8.2]. The lower cover, fixed to the pulley by means of $M4$ threaded rods, is equipped with a special housing for the lever of the release system.

The ratchet system [Figure 8.3] consists of:

- Ratchet wheel: made of *AISI* 316 steel, rigidly connected to the central shaft and equipped with eight teeth.
- Spring-loaded pawl: also made of *AISI* 316 steel, it prevents clockwise rotation. The release is made by a plug integral to the pawl, which extends through a dedicated housing in the lower cover.
- Central shaft: it is designed with a hole for the passage of the tensioning rope, accessible through dedicated openings in the lower cover. These openings facilitate precise manipulation of the shaft using a lever inserted into the hole.

However, the static friction discussed in chapter 7.1 prevents the rope from sliding along the pulley grooves. As a result, the system is ineffective, since the cable cannot be tensioned correctly, thus compromising the overall functioning of the mechanism.



Figure 8.1: Exploded view of the pulley

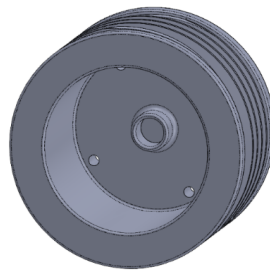


Figure 8.2: Internal view of the pulley

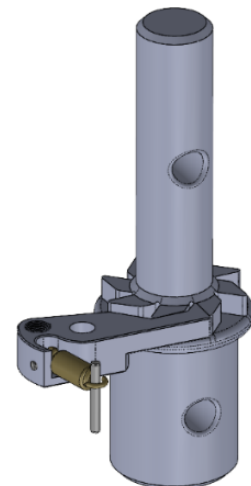


Figure 8.3: Ratchet system

8.2 Internal ratchet system

The pulley consists of two separate sections: a moving part and a fixed part.

- Moving part: attached to a *AISI* 316 steel band, to which the ratchet teeth, also made of *AISI* 316 steel, are fixed. This section acts as a dynamic element around which the rope to be tensioned is wrapped.
- Fixed part: it is the static support of the system and is the anchor point for the other rope, wrapped around it.

The configuration of the pulley varies between the right and left side, thus ensuring the correct tension of both ropes, as shown in [Figure 8.4]. With reference to the figure, we will call the pulley on the left *Pulley A* and the one on the right *Pulley B*.

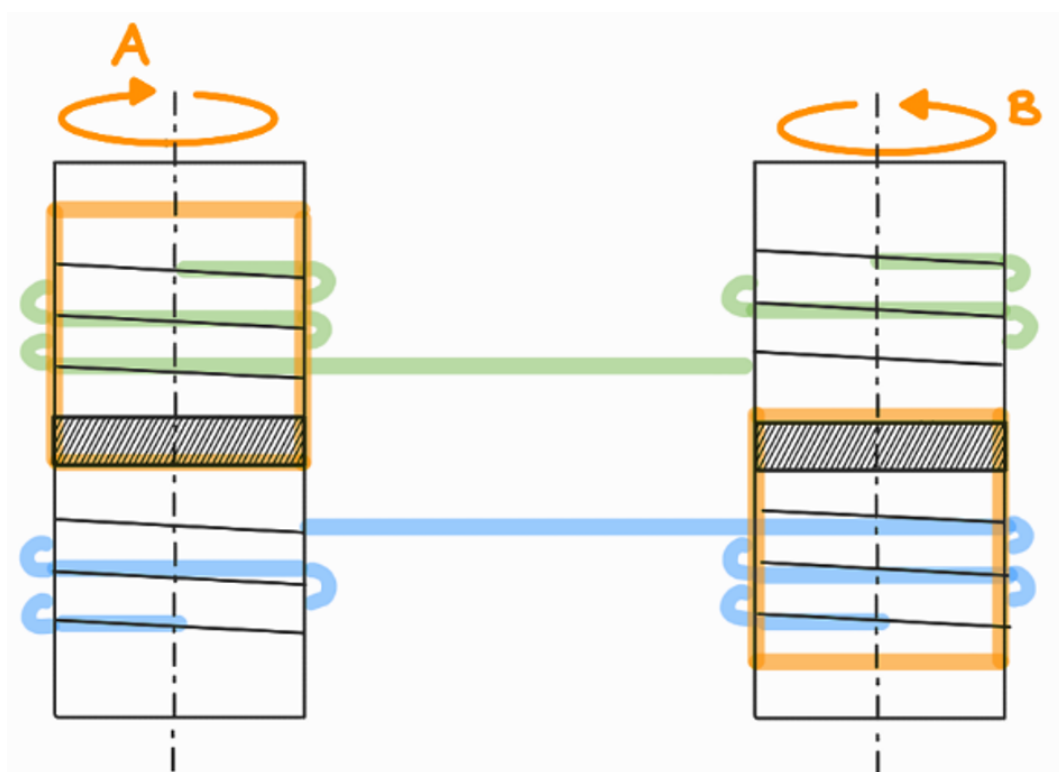


Figure 8.4: In orange, the moving part and the allowed rotation

8.2.1 Pulley A

Pulley A is designed to allow the upper rope to be tensioned clockwise and consists of:

- Moving part [Figure 8.5]: it has a hollow structure and is rigidly connected to the ratchet system described above, which allows the locking and controlled release of the rope.
- Upper cover [Figure 8.6]: rigidly connected to the shaft that connects the moving part to the fixed section of the pulley. It includes a dedicated housing for the rotation of the moving part, ensuring its correct operation.
- Lower cover [Figure 8.7]: rigidly connected to the fixed part of the pulley and equipped with a housing for the release system lever, necessary for releasing the tension of the rope.



Figure 8.5: Ratchet system of *Pulley A*

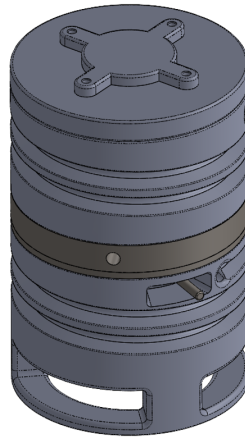


Figure 8.6: Upper view of of *Pulley A*

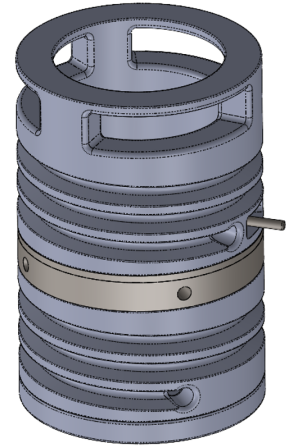


Figure 8.7: Lower view of of *Pulley A*

8.2.2 Pulley B

Pulley B is designed for tensioning the cable in a counter-clockwise direction and has a different structural configuration than *Pulley A*:

- Moving part [Figure 8.8]: characterised by a hollow lower structure and is rigidly connected to the ratchet system, similar to the one of *Pulley A*.
- Upper cover [Figure 8.9]: rigidly connected to the fixed part of the pulley and equipped with a housing for the lever of the release system.

- Lower cover [Figure 8.10]: rigidly connected to the shaft that the movable part to the fixed pulley section. It has a specific housing for the rotation of the moving part, ensuring its correct movement.

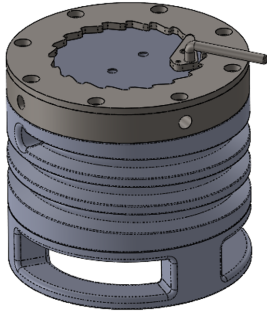


Figure 8.8: Exploded view of the pulley

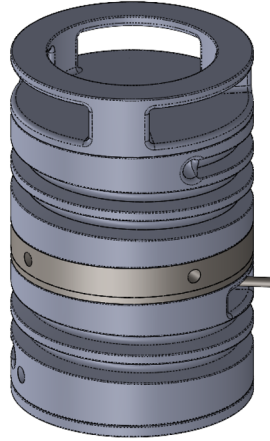


Figure 8.9: Internal view of the pulley

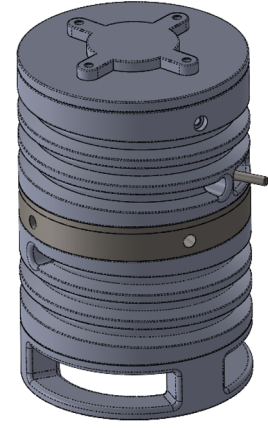


Figure 8.10: Ratchet system

Unlike *Pulley A*, in *Pulley B* the fixed part of the pulley and the upper cover do not form a single body: this separation is necessary to ease the assembly of the tensioning system. This configuration involves the integration of a central shaft to connect the two sections, resulting in a significant increase in weight compared to *Pulley A*.

8.2.3 Design of the ratchet system

The number of teeth has been chosen based on the rope's tensioning arc. Since the system operates in a discrete manner, we can easily assume that more teeth allow for a smaller pitch, improving tensioning accuracy and reducing the effort required to drive the ratchet.

In order to optimize these aspects, 20 teeth were selected.

The pawl was designed according to the tooth geometry, ensuring proper contact with the radial surface of the tooth to prevent unintended rotation.

It is assumed that a tensile load of 40 kg is applied to the rope. The force acting on the rope, considering gravitational acceleration, is:

$$F_R = 40 \cdot 9.81 = 392.4 \text{ N} \quad (8.1)$$

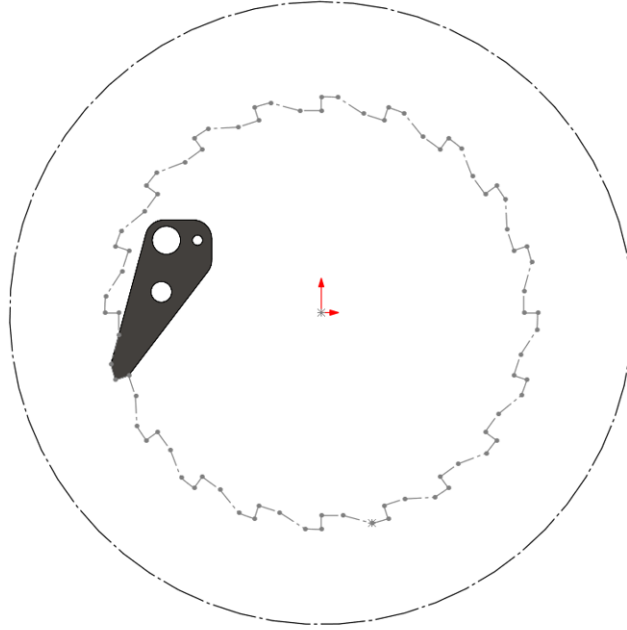


Figure 8.11: CAD scheme of the ratchet system

This force acts at a radius of $R_R = 45$ mm, while the force applied to a single tooth of the ratchet system acts at a smaller radius $r_D = 33.61$ mm. This value is obtained from the CAD model shown in [Figure 8.11].

By applying the principle of moment equilibrium:

$$F_D \cdot r_D = F_R \cdot R_R \quad (8.2)$$

$$F_D = \frac{F_R \cdot R_R}{r_D} = 525.38 \text{ N} \quad (8.3)$$

This is the force transmitted to the pawl, which must oppose an equal and opposite force to prevent the rotation of the ratchet wheel.

In addition to this force, the pawl is subjected to a second force, F_L , generated by the constraint reaction between the pawl itself and the housing in which it is seated. This force can be considered as the normal component of the constraint reaction between the contact surfaces of the tooth and the pawl.

With reference to [Figure 8.12], the distances from the centre of rotation of the pawl are obtained from the CAD model:

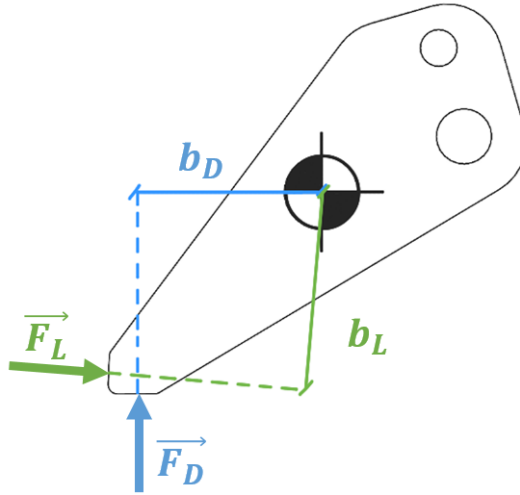


Figure 8.12: Pawl scheme

$$b_D = 10.09 \text{ mm}, \quad b_L = 10.07 \text{ mm} \quad (8.4)$$

By applying again the principle of moment equilibrium:

$$F_L \cdot b_L = F_D \cdot b_D \quad (4b.3.4) \quad (8.5)$$

$$F_L = \frac{F_D \cdot b_D}{b_L} = 526.42 \text{ N} \quad (4b.3.5) \quad (8.6)$$

This force represents the constraint reaction that the pawl must withstand within its housing to prevent the rotation of the system.

The verification of the pawl was carried out through FEM analysis on *SolidWorks*, applying the forces F_D and F_L just computed.

The stress analysis shown in [Figure 8.13] highlights that the maximum stress is concentrated at the tip of the pawl, with a value of 112.7 MPa. This value is significantly lower than the yield strength of *AISI 316* steel, confirming that the pawl is structurally capable of withstanding the load without the risk of failure.

The displacement analysis in [Figure 8.14] shows a maximum displacement of 2.14×10^{-3} mm along the radial direction of the tooth. This extremely small value indicates that the pawl maintains a stable position during operation, with negligible

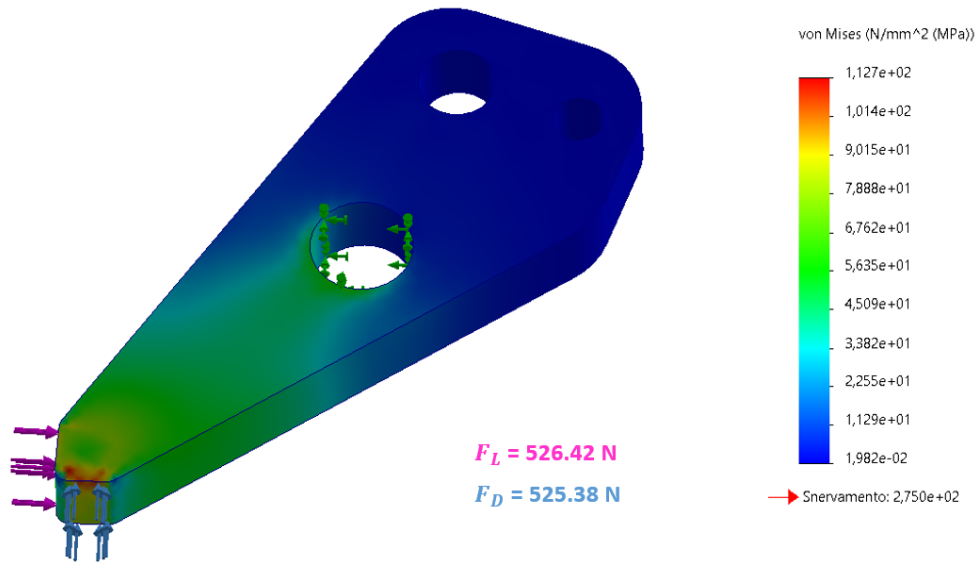


Figure 8.13: Stress analysis of the pawl [MPa]

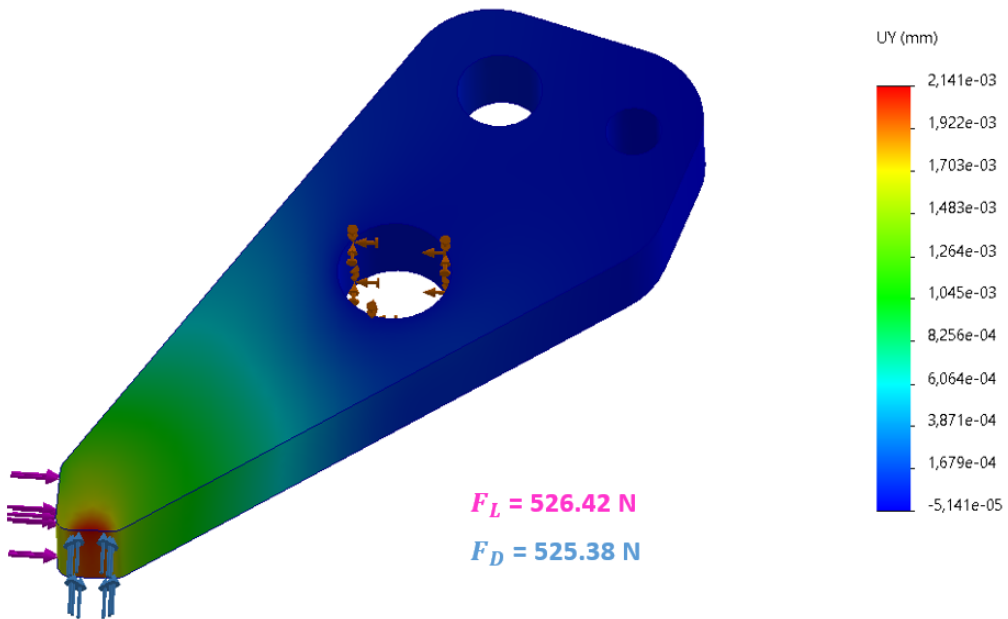


Figure 8.14: Displacement of the pawl along the radial direction of the tooth [mm]

deformations that do not compromise its ability to lock the pulley's rotation.

The FEM analysis thus confirms that the designed ratchet system is effective and reliable. The pawl can easily support the applied stresses, ensuring the locking of the pulley's rotation with minimal deformations. These results validate the component's design and confirm its suitability for the intended application.

Chapter 9

Final considerations

9.1 Pulley manufacturing

The metal components of the pulleys [Figure 9.1] are manufactured using laser cutting and drilling. In order to realize the pawl of the tensioning system, welding and bending operations were included. The material used is *AISI 316* stainless steel, known for its high corrosion resistance, making it particularly efficient in humid and marine environments.

All fastening elements, including screws, washers, nuts and threaded rods, are also made of *AISI 316* stainless steel.

The remaining parts [Figure 9.2] are produced using 3D printing with *Fused Deposition Modelling* (FDM) technology, utilizing *ABS CF100*, which provides an excellent combination of lightweight properties and mechanical strength.

The final result can be seen in [Figure 9.3] and [Figure 9.4].

9.2 Final testing

We repeated the test from chapter 7.1: the joint fixed to Pulley *A* (on the left in [Figure 9.5]) was held still while simulating the presence of an external disturbance by applying a force F_d at distance $b_d = 115$ mm from the rotation axis of the other joint, as illustrated in [Figure 7.3]. The force was applied at different intervals and the joint opening was measured in degrees using an encoder. The purpose of this test was to evaluate the failure behaviour of the rope and pulleys.

The results are shown in table 9.1.



Figure 9.1: Metal components of the pulleys



Figure 9.2: 3D printing of the components of the pulleys

Force to open the joint [kg]	Force applied on the rope [kg]	Joint opening [°]
0.00	0.00	0.272
3.80	9.71	1.503
8.20	20.95	6.513
12.90	32.97	10.380
17.00	43.44	13.368
23.70	60.57	17.059
28.30	72.32	19.257
28.10	71.80	13.104

Table 9.1: Final test

The tests were conducted without a specific preload, as it could not be accurately quantified.

- The first six tests were performed using a loading and unloading cycle, revealing significant joint displacement (18.985°), which made it necessary to re-tension the rope. The preload decreased considerably, although it could not be precisely



Figure 9.3: Assembled *Pulley A* (on the right) and *Pulley B* (on the left)



Figure 9.4: *Pulley A* assembled on RUVIFIST for the final test

quantified in the current setup.

- In the seventh and final test, conducted by directly applying the maximum load of approximately 31 Nm, a significant improvement in joint stability was observed (12.832°), confirming that the joint is highly sensitive to loading and unloading cycles.

It is important to emphasize that this test represents an extreme scenario, where one joint is locked while the other is free. In a real operational setting, the impact would be dampened by the symmetric opening of the opposite joint, ensuring a quick restoration of the initial symmetry.

Therefore, while the test highlights a temporary loss of symmetry, it is quickly restored, and this behavior is not typically expected under standard operating conditions. However, there remains a potential risk of derailment, due to the significant slack that the rope may experience in working conditions.

This issue can be mitigated by performing a series of tests as shown in chapter 7.1, where after each test cycle, the cable was further tensioned, reducing its slack.

During marine environment tests, it is essential to ensure proper rope tensioning, which can be manually verified, to guarantee optimal performance and minimize the risk of system malfunctions.



Figure 9.5: Final configuration of *Pulley A* and *Pulley B*

Chapter 10

Conclusions

This study has provided a comprehensive analysis of RUVIFIST's trajectory tracking performance using the Fossen simulation model. The evaluation of four different trajectories has offered key insights into the effectiveness of the PID controller and LOS driving strategy modelled, revealing strengths and weaknesses requiring improvement.

The results from the straight-line trajectory demonstrated that the controller influences force application as it corrects positional errors. Real-world implementation would benefit from motor inertia effects, which naturally smooth out sudden force changes.

In a similar way, the L-shaped trajectory highlighted the necessity of proper vehicle alignment before movement, due to the constraints imposed by the TCM. A small loss of trajectory precision was observed at the 90° turn due to rotational momentum, but this deviation could be mitigated with a more refined PID tuning. The analysis of the curved trajectory highlights the challenges posed by vehicle inertia: high kinetic energy from the straight segment resulted in trajectory drift during the turn, requiring corrective forces that led to deviations. This suggests that more sophisticated control strategies, such as feedforward compensation or MPC, could enhance path-following accuracy by anticipating dynamic effects.

The S-path trajectory, being the most complex, revealed a slight loss of tracking precision due to the compounded effects of inertia and control response limitations. However, the achieved trajectory remained closely aligned with the reference path, demonstrating the robustness of the control approach. Further refinement through optimized PID parameters and predictive control methods could enhance trajectory tracking accuracy and responsiveness.

Overall, while RUVIFIST demonstrated the ability to follow predefined paths with reasonable accuracy, the study highlights key areas for improvement. Future work should focus on implementing advanced control methodologies to refine force application and ensure optimal performance under real-world operational conditions.

The second part of this research focused on evaluating the mechanical resilience of the designed reconfiguration system, particularly the behaviour of the pulley mechanism under external disturbances. Experimental tests were conducted by applying a force at a specific distance while keeping one joint fixed, simulating extreme operating conditions.

The results showed that repeated loading and unloading cycles caused significant joint displacement, leading to rope slack that required re-tensioning. However, when the maximum load was applied in a single step, joint stability improved significantly. These findings emphasize the importance of maintaining optimal rope tension to prevent excessive slack and ensure the structural efficiency of the system. Although the test conditions were extreme, real-world operations would likely mitigate these effects due to the symmetric opening of the opposite joint, which naturally helps restore balance.

A crucial future development involves modifying the pulley design to serve a dual function: in addition to their primary role in the mechanism, the pulleys will also act as new structural supports for RUVIFIST. This adaptation is necessary due to the integration of additional downward-protruding sensors, which require a stable base to prevent interference during operations. Additionally, these modifications will accommodate the potential installation of robotic arms or other appendages that could enhance the vehicle's operational versatility.

Future testing should also include real-world assessments of the fully assembled vehicle under different intermediate configurations. By introducing controlled disturbances, these tests will help evaluate the system's true resilience and effectiveness in maintaining stability during reconfiguration. This step is essential to validate the mechanism's performance in realistic marine environments and ensure its reliability in practical applications.

Appendix A

Rigid-Body dynamics

A.1 Newton-Euler formulation

Linear dynamics

Given ρ as the density of a particle of volume dV of a rigid body \mathcal{B} , ρdV is the corresponding mass denoted by the position vector p in an inertial frame $O - xyz$. Given $V_{\mathcal{B}}$ as the body volume, the total mass is expressed as:

$$m = \int_{V_{\mathcal{B}}} \rho dV \quad (\text{A.1})$$

While the center of mass of \mathcal{B} and the linear momentum of the body \mathcal{B} can be defined as follows:

$$\mathbf{p}_C = \frac{1}{m} \int_{V_{\mathcal{B}}} \mathbf{p} \rho dV \quad (\text{A.2})$$

$$\mathbf{l} = \int_{V_{\mathcal{B}}} \dot{\mathbf{p}} \rho dV = m \dot{\mathbf{p}}_C \quad (\text{A.3})$$

Being the force the derivative of linear momentum, for a system with constant mass, it is possible to simplify the Newton's law of motion into the Newton's equations of motions:

$$\mathbf{f} = \dot{\mathbf{l}} = m \frac{d}{dt} \dot{\mathbf{p}}_C \quad (\text{A.4})$$

$$\mathbf{f} = m \ddot{\mathbf{p}}_C \quad (\text{A.5})$$

where:

- \mathbf{f} is the resultant of the external forces expressed in the Body frame $\{b\}$
- $\ddot{\mathbf{p}}_C$ is the acceleration of the center of gravity (CG)

Attitude dynamics

Consider now a rigid body rotating with respect to an inertial reference frame, with angular velocity $\boldsymbol{\omega} = \omega_1 \mathbf{b}_1 + \omega_2 \mathbf{b}_2 + \omega_3 \mathbf{b}_3$.

With reference to [Figure A.1], for a particle of mass m_i of the body it is possible to write the followings:

$$\mathbf{p}_i = X \hat{\mathbf{i}}_1 + Y \hat{\mathbf{i}}_2 + Z \hat{\mathbf{i}}_3 \quad (\text{A.6})$$

$$\mathbf{p}_C = X_o \hat{\mathbf{i}}_1 + Y_o \hat{\mathbf{i}}_2 + Z_o \hat{\mathbf{i}}_3 \quad (\text{A.7})$$

$$\mathbf{r}_i = x \hat{\mathbf{b}}_1 + y \hat{\mathbf{b}}_2 + z \hat{\mathbf{b}}_3 \quad (\text{A.8})$$

$$\dot{\mathbf{r}}_i^B = \dot{x} \hat{\mathbf{b}}_1 + \dot{y} \hat{\mathbf{b}}_2 + \dot{z} \hat{\mathbf{b}}_3 \quad (\text{A.9})$$

$$\mathbf{p}_i = \mathbf{p}_C + \mathbf{r}_i \quad (\text{A.10})$$

where:

- $\hat{\mathbf{i}}_j$, $j = 1,2,3$ are the unit vectors of the Inertial frame (IF)
- $\hat{\mathbf{b}}_j$, $j = 1,2,3$ are the unit vectors of the Body-fixed frame (BF)

In order to get the velocity of the particle in the Inertial frame, the computation of the derivative of (A.10) is needed.

The derivative of the first term \mathbf{p}_C is just $\dot{\mathbf{p}}_C$ as it is expressed in the Inertial frame, while the derivative of the second term \mathbf{r}_i is computed as:

$$\frac{d\mathbf{r}_i}{dt} = \left(\frac{dx}{dt} \hat{\mathbf{b}}_1 + \frac{dy}{dt} \hat{\mathbf{b}}_2 + \frac{dz}{dt} \hat{\mathbf{b}}_3 \right) + \left(x \frac{d\hat{\mathbf{b}}_1}{dt} + y \frac{d\hat{\mathbf{b}}_2}{dt} + z \frac{d\hat{\mathbf{b}}_3}{dt} \right) \quad (\text{A.11})$$

where:

- the first bracket represents the variation of velocity in time
- the second bracket is the variation of velocity due to the axes rotation, according to the *Coriolis's Theorem*

It is worth noting that, since we are referring to the Inertial Frame, the unit vectors $\hat{\mathbf{b}}_j$, $j = 1,2,3$ are considered non constants during the derivation as the Body-fixed frame moves with respect to the Inertial frame.

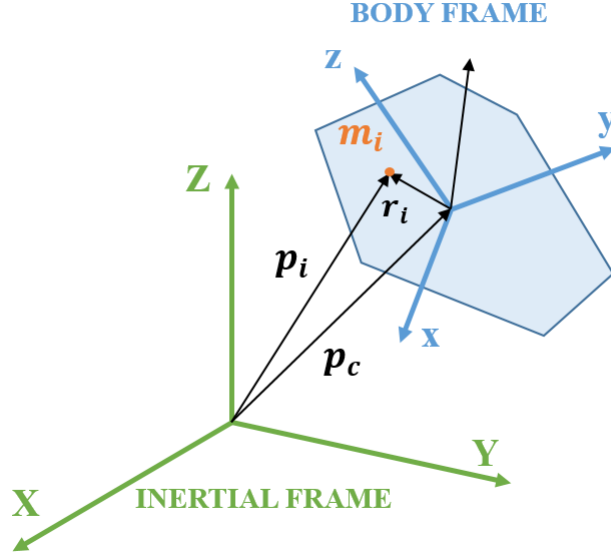


Figure A.1: Kinematics of a particle of the rigid body

Recalling the *Poisson's Theorem*, there exists one and only one vector $\boldsymbol{\omega}$ for which the following equations hold:

$$\frac{d\hat{\mathbf{b}}_1}{dt} = \boldsymbol{\omega} \times \hat{\mathbf{b}}_1, \quad \frac{d\hat{\mathbf{b}}_2}{dt} = \boldsymbol{\omega} \times \hat{\mathbf{b}}_2, \quad \frac{d\hat{\mathbf{b}}_3}{dt} = \boldsymbol{\omega} \times \hat{\mathbf{b}}_3 \quad (\text{A.12})$$

Thus, combining these equations into equation (A.11), it is possible to write the derivative of equation (A.10) as:

$$\dot{\mathbf{p}}_i = \dot{\mathbf{p}}_C + \dot{\mathbf{r}}_i^b + \boldsymbol{\omega} \times \mathbf{r}_i \quad (\text{A.13})$$

Consider the rigid body as a system of N particles with a total mass $m = \sum_i^N m_i$. The center of mass CG is defined as:

$$\mathbf{p}_C = \frac{1}{m} \sum_{i=1}^N m_i \mathbf{p}_i \quad (\text{A.14})$$

This equation can be rearranged to obtain the following property:

$$\sum_{i=1}^N m_i (\mathbf{p}_i - \mathbf{p}_C) = \sum_{i=1}^N m_i \mathbf{r}_i = 0 \quad (\text{A.15})$$

We now compute the *Angular momentum* (i.e. moment of momentum) of a particle i as follows:

$$\mathbf{H}_i \doteq \mathbf{r}_i \times m_i \dot{\mathbf{p}}_i = \mathbf{r}_i \times m_i (\dot{\mathbf{p}}_C + \dot{\mathbf{r}}_i^b + \boldsymbol{\omega} \times \mathbf{r}_i) \quad (\text{A.16})$$

Being $\dot{\mathbf{r}}_i^B = 0$ for the rigid body and remembering the property of the cross product $\mathbf{a} \times \mathbf{b} = -\mathbf{b} \times \mathbf{a}$, it is possible to rewrite the *Angular momentum*:

$$\begin{aligned} \mathbf{H}_i &= \mathbf{r}_i \times m_i (\dot{\mathbf{p}}_C + \boldsymbol{\omega} \times \mathbf{r}_i) \\ &= -\dot{\mathbf{p}}_C \times m_i \mathbf{r}_i + \mathbf{r}_i \times m_i (\boldsymbol{\omega} \times \mathbf{r}_i) \end{aligned} \quad (\text{A.17})$$

The *Angular momentum* of the entire body is:

$$\begin{aligned} \mathbf{H} &= -\sum_{i=1}^N \dot{\mathbf{p}}_C \times m_i \mathbf{r}_i + \sum_{i=1}^N \mathbf{r}_i \times m_i (\boldsymbol{\omega} \times \mathbf{r}_i) \\ &= -\dot{\mathbf{p}}_C \times \sum_{i=1}^N m_i \mathbf{r}_i + \sum_{i=1}^N \mathbf{r}_i \times m_i (\boldsymbol{\omega} \times \mathbf{r}_i) \end{aligned} \quad (\text{A.18})$$

According to the property of equation (A.15) it is possible to rewrite (A.18) as:

$$\mathbf{H} = \sum_{i=1}^N \mathbf{r}_i \times (\boldsymbol{\omega} \times \mathbf{r}_i) m_i \quad (\text{A.19})$$

and in continuous form:

$$\mathbf{H} = \int_{V_B} \mathbf{r} \times (\boldsymbol{\omega} \times \mathbf{r}) dm. \quad (\text{A.20})$$

Remembering the property of the cross product $\mathbf{a} \times (\mathbf{b} \times \mathbf{c}) = (\mathbf{a} \cdot \mathbf{c}) \mathbf{b} - (\mathbf{a} \cdot \mathbf{b}) \mathbf{c}$, we have that:

$$\mathbf{r} \times (\boldsymbol{\omega} \times \mathbf{r}) = (\mathbf{r} \cdot \mathbf{r}) \boldsymbol{\omega} - (\mathbf{r} \cdot \boldsymbol{\omega}) \mathbf{r} = (\mathbf{1}r^2 - \mathbf{r}\mathbf{r}^T) \boldsymbol{\omega} \quad (\text{A.21})$$

It is then possible to rewrite equation (A.20) as follows:

$$\mathbf{H} = \begin{bmatrix} I_x & I_{xy} & I_{xz} \\ I_{yx} & I_y & I_{yz} \\ I_{zx} & I_{zy} & I_z \end{bmatrix} \begin{bmatrix} \omega_1 \\ \omega_2 \\ \omega_3 \end{bmatrix} = \mathbf{I} \boldsymbol{\omega} \quad (\text{A.22})$$

where \mathbf{I} is the *Inertia matrix* (or *Inertia tensor*). Its terms are computed as shown below:

Moments of Inertia	Products of Inertia
$I_x = \int_{V_B} (y^2 + z^2) dm$	$I_{xy} = I_{yx} = - \int_{V_B} xy dm$
$I_y = \int_{V_B} (x^2 + z^2) dm$	$I_{xz} = I_{zx} = - \int_{V_B} xz dm$
$I_z = \int_{V_B} (x^2 + y^2) dm$	$I_{yz} = I_{zy} = - \int_{V_B} yz dm$

Now let's suppose that a moment \mathbf{m} is acting on the body \mathcal{B} . The second law of dynamics for a rotating body is:

$$\dot{\mathbf{H}} = \mathbf{m}. \quad (\text{A.23})$$

A derivation of A.22 is then needed.

The *Inertia matrix* is considered as a constant matrix, while the derivative of $\boldsymbol{\omega}$ in the Inertial frame is given by:

$$\dot{\boldsymbol{\omega}} = \dot{\boldsymbol{\omega}}^b + \boldsymbol{\omega} \times \boldsymbol{\omega}^b \quad (\text{A.24})$$

The derivative of the *Angular momentum* (A.18) is thus computed as:

$$\dot{\mathbf{H}} = \mathbf{I}\dot{\boldsymbol{\omega}}^b + \boldsymbol{\omega} \times \mathbf{I}\boldsymbol{\omega}^b. \quad (\text{A.25})$$

Replacing (A.25) in (A.23), it is possible to get the *Euler's moment* equation:

$$\mathbf{I}\dot{\boldsymbol{\omega}}^b + \boldsymbol{\omega} \times \mathbf{I}\boldsymbol{\omega}^b = \mathbf{m}. \quad (\text{A.26})$$

The *Euler's moment* equation is expressed in the Body-fixed frame $\{b\}$, while the inertia matrix is computed about CG (i.e. in the Inertial frame).

A.2 Equation of Motion

In the study of rigid-body dynamics, computations are initially performed around the center of gravity CG, due to its simplicity in deriving translational motion equations and defining the inertia matrix. This approach simplifies the analysis and application of the Newton's laws discussed in the previous section.

Once the motion equations are established, they are then transformed to the geometric center CO, which is often chosen in marine craft to facilitate more effective control system design and optimize performance.

Motion about CG

From equation (A.5) it follows that:

$$\mathbf{f}^b = \frac{d}{dt} (m\mathbf{v}_C^b) = m (\dot{\mathbf{v}}_C^b + \boldsymbol{\omega}^b \times \mathbf{v}_C^b) \quad (\text{A.27})$$

Now, remember the cross product operator, defined by:

$$\boldsymbol{\lambda} \times \mathbf{a} \doteq \mathbf{S}(\boldsymbol{\lambda})\mathbf{a} \quad (\text{A.28})$$

where \mathbf{S} is a *skew-symmetric* matrix ($\mathbf{S} = -\mathbf{S}^T$) defined as:

$$\mathbf{S}(\boldsymbol{\lambda}) = -\mathbf{S}^T(\boldsymbol{\lambda}) = \begin{bmatrix} 0 & -\lambda_3 & \lambda_2 \\ \lambda_3 & 0 & -\lambda_1 \\ -\lambda_2 & \lambda_1 & 0 \end{bmatrix} \quad (\text{A.29})$$

It is possible to rewrite equations (A.28) and (A.29) as:

$$m \left[\dot{\mathbf{v}}_C^b + \mathbf{S}(\boldsymbol{\omega}^b) \mathbf{v}_C^b \right] = \mathbf{f}^b \quad (\text{A.30})$$

$$\mathbf{I} \dot{\boldsymbol{\omega}}^b - \mathbf{S}(\mathbf{I}\boldsymbol{\omega}) \boldsymbol{\omega}^b = \mathbf{m}^b \quad (\text{A.31})$$

The *Newton–Euler* equations (A.30) and (A.31) can be represented in matrix form according to:

$$\mathbf{M}_{RB}^{CG} \dot{\boldsymbol{\nu}} + \mathbf{C}_{RB}^{CG} \boldsymbol{\nu} = \boldsymbol{\tau} \quad (\text{A.32})$$

$$\begin{bmatrix} m\mathbf{1}_{3 \times 3} & \mathbf{0}_{3 \times 3} \\ \mathbf{0}_{3 \times 3} & \mathbf{I} \end{bmatrix} \begin{bmatrix} \dot{\mathbf{v}}_C^b \\ \dot{\boldsymbol{\omega}}^b \end{bmatrix} + \begin{bmatrix} m\mathbf{S}(\boldsymbol{\omega}^b) & \mathbf{0}_{3 \times 3} \\ \mathbf{0}_{3 \times 3} & -\mathbf{S}(\mathbf{I}\boldsymbol{\omega}) \end{bmatrix} \begin{bmatrix} \mathbf{v}_C^b \\ \boldsymbol{\omega}^b \end{bmatrix} = \begin{bmatrix} \mathbf{f}^b \\ \mathbf{m}^b \end{bmatrix} \quad (\text{A.33})$$

Motion about CO

The equations of motion about CG need to be transformed into equations about CO using a coordinate transformation:

$$\begin{aligned} \mathbf{v}_C^b &= \mathbf{v}_O^b + \boldsymbol{\omega}^b \times \mathbf{p}_C^b \\ &= \mathbf{v}_C^b - \mathbf{p}_C^b \times \boldsymbol{\omega}^b \\ &= \mathbf{v}_C^b + \mathbf{S}^T(\mathbf{p}_C^b) \boldsymbol{\omega}^b \end{aligned} \quad (\text{A.34})$$

It follows that:

$$\begin{bmatrix} \mathbf{v}_C^b \\ \boldsymbol{\omega}^b \end{bmatrix} = \mathbf{H}(\mathbf{p}_C^b) \begin{bmatrix} \mathbf{v}_O^b \\ \boldsymbol{\omega}^b \end{bmatrix} \quad (\text{A.35})$$

where $\mathbf{H}(\mathbf{p}_C^b) \in \mathbb{R}^{3 \times 3}$ is a transformation matrix, given by:

$$\mathbf{H}(\mathbf{p}_C^b) \doteq \begin{bmatrix} \mathbf{1}_{3 \times 3} & \mathbf{S}^T(\mathbf{p}_C^b) \\ \mathbf{0}_{3 \times 3} & \mathbf{1}_{3 \times 3} \end{bmatrix} \quad (\text{A.36})$$

It should be noted that the angular velocity remains unchanged during this transformation.

The next step is to transform (A.33) from CG to CO using (A.35):

$$\mathbf{H}^T(\mathbf{p}_C) \mathbf{M}_{RB}^{CG} \mathbf{H}(\mathbf{p}_C) \begin{bmatrix} \dot{\mathbf{v}}_O^b \\ \dot{\boldsymbol{\omega}}^b \end{bmatrix} + \mathbf{H}^T(\mathbf{p}_C) \mathbf{C}_{RB}^{CG} \mathbf{H}(\mathbf{p}_C) \begin{bmatrix} \mathbf{v}_O^b \\ \boldsymbol{\omega}^b \end{bmatrix} = \mathbf{H}^T(\mathbf{p}_C) \begin{bmatrix} \mathbf{f}^b \\ \mathbf{m}^b \end{bmatrix} \quad (\text{A.37})$$

We now define two new matrices in CO according to the following:

$$\mathbf{M}_{RB}^{CO} \doteq \mathbf{H}^T(\mathbf{p}_C) \mathbf{M}_{RB}^{CG} \mathbf{H}(\mathbf{p}_C) \quad (\text{A.38})$$

$$(\text{A.39})$$

$$\mathbf{C}_{RB}^{CO} \doteq \mathbf{H}^T(\mathbf{p}_C) \mathbf{C}_{RB}^{CG} \mathbf{H}(\mathbf{p}_C) \quad (\text{A.40})$$

Expanding these expressions gives the following results:

$$\begin{aligned} \mathbf{M}_{RB}^{CO} &= \begin{bmatrix} m\mathbf{1}_{3 \times 3} & -m\mathbf{S}(\mathbf{p}_C^b) \\ m\mathbf{S}(\mathbf{p}_C^b) & \mathbf{I}_o \end{bmatrix} \\ &= \begin{bmatrix} m & 0 & 0 & 0 & mz_C & -my_C \\ 0 & m & 0 & -mz_C & 0 & mx_C \\ 0 & 0 & m & my_C & -mx_C & 0 \\ 0 & -mz_C & my_C & I_x & -I_{xy} & -I_{xz} \\ mz_C & 0 & -mx_C & -I_{yx} & I_y & -I_{yz} \\ -my_C & mx_C & 0 & -I_{zx} & -I_{zy} & I_z \end{bmatrix} \quad (\text{A.41}) \end{aligned}$$

$$\mathbf{C}_{RB}^{CO} = \begin{bmatrix} m\mathbf{S}(\boldsymbol{\omega}^b) & -m\mathbf{S}(\boldsymbol{\omega}^b) \mathbf{S}(\mathbf{p}_C^b) \\ m\mathbf{S}(\mathbf{p}_C^b) \mathbf{S}(\boldsymbol{\omega}^b) & -\mathbf{S}(\mathbf{I}_o \boldsymbol{\omega}^b) \end{bmatrix} \quad (\text{A.42})$$

Bibliography

- [1] Mirco Vangi, Edoardo Topini, Gherardo Liverani, Alberto Topini, Alessandro Ridolfi, and Benedetto Allotta. «Design, Development, and Testing of an Innovative Autonomous Underwater Reconfigurable Vehicle for Versatile Applications». In: *IEEE Journal of Oceanic Engineering* (2025) (cit. on p. 5).
- [2] Mirco Vangi, Edoardo Topini, Gherardo Liverani, Alessandro Ridolfi, and Benedetto Allotta. «Navigation and control systems for a reconfigurable underwater vehicle for inspection, free-floating intervention and survey tasks». In: *2023 IEEE International Workshop on Metrology for the Sea; Learning to Measure Sea Health Parameters (MetroSea)*. IEEE, 2023, pp. 545–550 (cit. on p. 5).
- [3] EDOARDO TOPINI. «Underwater reconfigurable vehicles for survey, inspection and intervention». In: (2024) (cit. on p. 5).
- [4] Marco Pagliai et al. «Design and testing of innovative thrusters and their integration in the design of a reconfigurable underwater vehicle». In: (2019) (cit. on p. 5).
- [5] Benedetto Allotta, Jonathan Gelli, Marco Pagliai, and Alessandro Ridolfi. *Underwater vehicle with variable configuration*. US Patent 11,505,293. Nov. 2022 (cit. on p. 5).
- [6] Thor I. Fossen. *Handbook of Marine Craft Hydrodynamics and Motion Control*. John Wiley & Sons, 2011 (cit. on pp. 9, 19).
- [7] Fjellstad and Fossen. «Quaternion feedback regulation of underwater vehicles». In: *1994 Proceedings of IEEE International Conference on Control and Applications*. IEEE, 1994, pp. 857–862 (cit. on p. 15).
- [8] E.O. Diaz. *3d Motion of Rigid Bodies - A Foundation for Robot Dynamics Analysis*. Springer, 2019 (cit. on p. 19).
- [9] G. Antonelli. *Underwater Robots - Motion and Force Control of Vehicle-Manipulator Systems*. Springer, 2006 (cit. on p. 19).

- [10] Thor I Fossen. «How to incorporate wind, waves and ocean currents in the marine craft equations of motion». In: *IFAC Proceedings Volumes* 45.27 (2012), pp. 126–131 (cit. on p. 23).
- [11] Enrico Anderlini, Gordon G Parker, and Giles Thomas. «Control of a ROV carrying an object». In: *Ocean Engineering* 165 (2018), pp. 307–318 (cit. on p. 23).
- [12] Edoardo Topini, Marco Pagliai, and Benedetto Allotta. «Dynamic maneuverability analysis: A preliminary application on an autonomous underwater reconfigurable vehicle». In: *Applied Sciences* 11.10 (2021), p. 4469 (cit. on p. 25).
- [13] <https://bluerobotics.com/store/thrusters/t100-t200-thrusters/t200-thruster-r2-rp/> (cit. on p. 28).
- [14] Anastasios M Lekkas and Thor I Fossen. «Line-of-sight guidance for path following of marine vehicles». In: *Advanced in marine robotics* 5 (2013), pp. 63–92 (cit. on p. 31).
- [15] Anastasios M Lekkas and Thor I Fossen. «Trajectory tracking and ocean current estimation for marine underactuated vehicles». In: *2014 IEEE Conference on Control Applications (CCA)*. IEEE. 2014, pp. 905–910 (cit. on p. 31).
- [16] <https://fibrx1.com/wp-content/uploads/2020/07/FibrXL-PDS-performance-0720-DEF-Dyneema.pdf> (cit. on p. 48).
- [17] Nicola P. Belfiore Augusto Di Benedetto Ettore Pennestrì. *Fondamenti di Meccanica Applicata alle Macchine*. Zanichelli, 2024 (cit. on p. 51).